HHS Public Access

Author manuscript

J Physiol. Author manuscript; available in PMC 2022 March 01.

Published in final edited form as:

J Physiol. 2021 March ; 599(6): 1833–1854. doi:10.1113/JP281014.

Biased auditory nerve central synaptopathy is associated with Age-related Hearing Loss

Meijian Wang[1], **Chuangeng Zhang**[1], **Shengyin Lin**[1], **Yong Wang**[1], **Benjamin J. Seicol**[1,3], **Robert W. Ariss**[2], **Ruili Xie**[1,3,*]

[1]Department of Otolaryngology – Head and Neck Surgery, The Ohio State University, Columbus, OH 43210, USA

[2]College of Medicine and Life Sciences, University of Toledo, Toledo, OH 43614, USA

[3]Department of Neuroscience, The Ohio State University, Columbus, OH 43210, USA

Abstract

Sound information is transmitted from the cochlea to the brain by different subtypes of spiral ganglion neurons (SGN), which show varying degrees of vulnerability under pathological conditions. Selective cochlear synaptopathy, the preferential damage of certain subtypes of SGN peripheral synapses, has been recognized as one of the main mechanisms of hearing loss. The organization and function of the auditory nerve (AN) central synapses from different subtypes of SGNs remain unclear, including how different AN synapses reassemble onto individual neurons in the cochlear nucleus (CN), and how they differentially change during hearing loss. Combining immunohistochemistry with electrophysiology, we investigated the convergence pattern and subtype-specific synaptopathy of AN synapses at the endbulb of Held, as well as the response properties of their postsynaptic bushy neurons in CBA/CaJ mice of either sex under normal hearing and age-related hearing loss (ARHL). We found that calretinin-expressing (type I_a) and non-calretinin-expressing (type I_b/I_c) endbulbs converged along a continuum of different ratios onto individual bushy neurons with varying physiological properties. Endbulbs degenerated during aging in parallel with ARHL. Furthermore, the degeneration was more severe in non-calretinin-expressing synapses, which correlated with a gradual decrease in bushy neuron subpopulation predominantly innervated by these inputs. These synaptic and cellular changes were profound in middle-aged mice when their hearing thresholds were still relatively normal and prior to severe ARHL. Our findings suggest that biased AN central synaptopathy and the correlated shift in CN neuronal composition play significant roles in weakened auditory input and altered central auditory processing during ARHL.

[*]**Corresponding author:** Ruili Xie; ruili.xie@osumc.edu.

Author Contributions

All experiments were performed in the Auditory Neuroscience Laboratory (PI: Ruili Xie) at The Ohio State University. R.X. designed the research; R.X., M.W., C.Z., S.L., and Y.W. acquired the data; M.W., R.X., B.J.S., and R.W.A. analyzed the data; R.X. drafted the paper; All authors edited and approved the final version of the paper. All authors qualify for authorship and agree to be accountable for the work.

Competing Interests:

The authors declare no competing financial interests.

Data Availability Statement

The data that support the findings of this study are available from the corresponding author upon reasonable request.

INTRODUCTION

Spiral ganglion neurons (SGN) of the peripheral auditory system convey sound information from sensory hair cells to the cochlear nucleus (CN) (Nayagam *et al.*, 2011), which is the first station of the central auditory system. Most SGNs (90–95%) are type I (Spoendlin, 1969; Kiang *et al.*, 1982) and can be further divided into three subtypes based on their spontaneous firing rate and threshold, fiber caliber and preferential terminal distribution around the hair cell basal circumference (Liberman, 1978, 1980, 1982b, a; Liberman & Oliver, 1984). These SGN subtypes differentially encode sound intensity, and collectively ensure a comprehensive representation of the acoustic environment. Transfer of sound information through the bipolar SGNs begins at their dendritic terminal of cochlear synapses on hair cells, and ends at AN central synapses in the CN (Nayagam *et al.*, 2011; Yu & Goodrich, 2014). Pathology of the cochlear synapses (known as “cochlear synaptopathy”) due to noise insult and aging preferentially affects the low spontaneous rate/high threshold subtype of type I SGNs (Furman *et al.*, 2013; Liberman *et al.*, 2015), and is recognized as a major mechanism that underlies hearing loss (Kujawa & Liberman, 2015; Liberman *et al.*, 2015; Liberman, 2017; Parthasarathy & Kujawa, 2018). However, it remains unknown how different subtypes of AN central synapses converge onto individual CN neurons (Spirou *et al.*, 2005; Nayagam *et al.*, 2011; Yu & Goodrich, 2014), how different innervation patterns correlate with postsynaptic neuronal response properties, and most importantly, how subtype-specific changes of AN synapses affect the neural processing of target CN neurons under pathological conditions. Research to answer these questions has been hindered by the lack of known markers that can specifically label different subtypes of type I SGNs. Recent studies using single-cell RNA sequencing technique reported various molecular markers that can selectively classify type I SGNs into three distinct subtypes (type I_a, I_b, and I_c) (Petitpre *et al.*, 2018; Shrestha *et al.*, 2018; Sun *et al.*, 2018). In particular, calretinin was shown to be selectively expressed in type I_a SGNs, whose peripheral synapses contact the pillar side of inner hair cells (Sharma *et al.*, 2018) and presumably give rise to auditory nerve (AN) fibers with high spontaneous rate/low threshold (Liberman, 1982b).

The most prominent AN synapse is the endbulb of Held (Ryugo & Fekete, 1982; Rouiller *et al.*, 1986), which reliably transmits information about the temporal fine structure of sound to its postsynaptic bushy neuron in ventral CN (Joris *et al.*, 1994a; Joris *et al.*, 1994b; Manis *et al.*, 2011). Such temporal information is crucial for pitch perception and speech recognition (Shannon *et al.*, 1995; Moore, 2008), which are often compromised in hearing impaired patients (Lorenzi *et al.*, 2006; Grose & Mamo, 2010; Anderson *et al.*, 2012). After hearing loss, endbulb of Held synapses show modified synaptic morphology with reduced size and simplified complexity (Ryugo *et al.*, 1997; Ryugo *et al.*, 1998; Wright *et al.*, 2014), as well as compromised synaptic transmission (Oleskevich & Walmsley, 2002; Wang & Manis, 2005; Wright *et al.*, 2014; Xie & Manis, 2017b; Zhuang *et al.*, 2017) and reduced auditory input to target neurons (Xie, 2016). Despite decades of research on the endbulbs of Held, however, it remains unknown how different subtypes of endbulbs converge onto individual bushy neurons, as well as whether and how such synaptic innervation changes during hearing loss. It is also unclear how subtype-specific changes of the endbulbs impact the response properties of postsynaptic bushy neurons.

To address these issues, we combined immunohistochemistry with electrophysiology using acute brain slices from CBA/CaJ mice at three different age groups with normal hearing, moderate ARHL that mimics hidden hearing loss, and prominent ARHL (Sergeyenko *et al.*, 2013). Endbulb of Held synapses from type I_a SGNs (high spontaneous rate/low threshold) were differentiated from other subtypes (type I_b/I_c SGNs with medium/low spontaneous rate and medium/high threshold) based on immunostaining against calretinin (Liberman, 1982b; Petitpre *et al.*, 2018; Sharma *et al.*, 2018; Shrestha *et al.*, 2018; Sun *et al.*, 2018). We report the innervation patterns of type I_a and non-type I_a endbulbs on individual bushy neurons and their intrinsic and AN-evoked response properties, as well as subtype-specific AN central synaptopathy during ARHL.

METHODS

Ethical Approval

All experiments were conducted under the guidelines of the protocols approved by the Institutional Animal Care and Use Committee of The Ohio State University (IACUC protocol number: 2018A00000055), which maintains an Animal Welfare Assurance (#D16–00168 / A3261–01) in compliance with the United States Public Health Service Policy on Humane Care and Use of Laboratory Animals. We understand the ethical principles under which the journal operates, and our work complies with the animal ethics checklist.

Origin and Source of the Animals

The study used CBA/CaJ mice of either sex, which were purchased from The Jackson Laboratory, bred and maintained at the animal facility at The Ohio State University. Three age groups of mice were used, including 32 young (1.5 – 4.5 months), 22 middle-aged (17 – 19 months), and 55 old (28 – 32 months) mice.

Access to Food and Water

All mice were maintained in 12-hour light/dark cycle, and had ad libitum access to food and water.

Anaesthetic Protocols and Euthanasia

Mice were deeply anaesthetized with IP injection of ketamine (100 mg/kg) and xylazine (10 mg/kg), which was verified by the absence of toe-pinch reflex. Euthanasia was performed under anesthesia by decapitation.

Auditory Brainstem Response (ABR)

Hearing status of the mice were assessed by measuring ABR to clicks as previously described (Wang *et al.*, 2019). Briefly, mice were anaesthetized and placed inside a sound-attenuating chamber. Body temperature was maintained at ~ 36 °C using a feedback-controlled heating pad. ABR to clicks were acquired using a RZ6-A-P1 system with BioSigRZ software (Tucker-Davis Technologies). Clicks (0.1 ms, monophasic with alternating phase; 21 times/s) were delivered through a free field MF1 magnetic speaker located 10 cm away from the pinna. Recording needle electrodes were placed at the

ipsilateral pinna and vertex, with the ground electrode at the rump. ABR at each sound level was repeated 512 times and averaged (Fig. 1).

Brain Slice Preparation

Under ketamine/xylazine anesthesia, mice were decapitated and the skulls were opened to retrieve the brainstem. Parasagittal slices containing the CN were cut at a thickness of 225 – 240 μm using a Vibratome 1000 (Technical Products, Inc.) or a VT1200S Microtome (Leica Biosystems). Tissue dissection and slicing were performed in artificial cerebral spinal fluid (ACSF) at 34 °C. ACSF contained (in mM): 122 NaCl, 3 KCl, 1.25 NaH_2PO_4, 25 $NaHCO_3$, 20 glucose, 3 *myo*-inositol, 2 sodium pyruvate, 0.4 ascorbic acid, 1.8 $CaCl_2$ and 1.5 $MgSO_4$, and was gassed with 95% O_2 and 5% CO_2. Slices were then incubated in the same ACSF at 34 °C for 30–45 minutes before recordings began.

Electrophysiological Recording

After incubation, the brain slice was moved to an ACSF-bathed recording chamber under an Axio Examiner microscope (Carl Zeiss). Whole-cell recordings under current clamp mode were performed from bushy neurons of the anteroventral CN (AVCN). Recording pipettes were made using a P-2000 micropipette puller (Sutter Instrument) and filled with electrode solution that contained (in mM): 126 potassium gluconate, 6 KCl, 2 NaCl, 10 HEPES, 0.2 EGTA, 4 MgATP, 0.3 GTP, 10 Tris-phosphocreatine, and pH adjusted to 7.20. Alexa Fluor 594 was added to the electrode solution at the final concentration of 0.01% by weight to dye-fill the neuron for online visualization of cell morphology as well as cell labeling upon completion. Data acquisition used hardware and software from Molecular devices, including Multiclamp 700B amplifier, Digidata 1550B acquisition system and pClamp 11 software. All recordings were made at 34 °C. Recordings were made from neurons in the middle and dorsal area of the AVCN. Only bushy neurons were included in the study, which were identified based on electrophysiological response properties and morphological features as previously described (Cant & Morest, 1979; Webster & Trune, 1982; Wu & Oertel, 1984; Manis *et al.*, 2019). Responses to current step injections were obtained to assess intrinsic membrane properties. AN stimulation (Fig. 2A) was delivered through a 75 μm diameter concentric stimulating electrode (Frederick Haer Company) placed at the nerve root. The stimulus pulse had a duration of 0.1 ms, with intensity set at ~30% above the threshold intensity level that first triggered spikes in the target neuron. For neurons that failed to fire any spikes, stimulus intensity was tested up to the level that would cause tissue damage at the stimulation site. Responses to trains of AN stimulation at 100 Hz for 9 s and at 400 Hz for 10 s were recorded. Liquid junction potential was - 12 mV and was corrected. After completion of data acquisition, the recording electrode was slowly withdrawn until it broke off from the target neuron, which usually resealed itself with preserved neuronal morphology and remained filled with Alexa Fluor 594 dye. The brain slice was immediately fixed in 4% paraformaldehyde in PBS for 15 minutes, followed by post-hoc immunohistochemistry.

Immunohistochemistry

Fixed brain slices with dye-filled neurons were processed for immunostaining as previously described (Karadottir & Attwell, 2006; Lin & Xie, 2019). After rinsing in PBS (3 times, 15

minutes each), slices were pre-incubated in blocking solution (10% horse serum, 0.5% Triton X-100, and 0.05% NaN_3 in PBS) for 6 hours at room temperature, followed by overnight incubation with primary antibodies against VGluT1 (guinea pig anti VGluT1; Cat# 135304, Synaptic Systems, 1:500) and calretinin (rabbit anti calretinin; Cat# 214102, Synaptic Systems, 1:500) at 4 °C. Slices were then rinsed again in PBS (4 times, 20 minutes each), incubated with secondary antibodies (goat anti guinea pig IgG, Alexa 488 conjugated, Cat # A11073, Thermo Fisher Scientific, 1:500; and goat anti rabbit IgG, Alexa 647 conjugated, Cat# A21245, Thermo Fisher Scientific, 1:500) at room temperature for 4 hours, re-rinsed, and mounted on slide with DAPI-Fluoromount-G mounting media (Southern Biotech). Filled neurons and labeled AN synapses were imaged using an Olympus FV3000 confocal microscope. Images were sampled using a 60x oil immersion objective, 3.0 times software zoom, a z-step size of 0.3 μm, and at a resolution of either 800 × 800 or 1024 × 1024 pixels.

Image processing

All image processing and measurement were performed age-blinded and done using Imaris software (version 9.5.0; Oxford Instruments). Three-dimensional reconstruction of the dye-filled target bushy neuron (magenta), VGluT1-labeled puncta (green) and type I_a endbulb of Held terminals (red) in close proximity to the soma of the target bushy neuron were made using semi-automated Imaris tools, including masking uninterested area and rendering surfaces in three separate channels (see Supplemental Video 1 for detailed step-by-step process). VGluT1-labeled puncta located inside type I_a endbulbs were determined as puncta from type I_a synapses and shown in yellow (overlap of red and green), while those outside of type I_a endbulbs were from non-type I_a synapses and remained in green (Fig. 2D–F, Supplemental Video 1). Volumes of VGluT1-labeled puncta and individually identified endbulb of Held synapses were measured.

Electrophysiology Analysis

Electrophysiological data were analyzed in Igor Pro (WaveMetrics) using custom-written functions. Responses to current step injections were used to quantify the intrinsic membrane properties as previously described (Xie & Manis, 2017a). Input resistance was calculated as the slope of the current-voltage relationship curve from current step injections of −25, −50, −75, and −100 pA and the resulted peak hyperpolarization amplitudes. Depolarizing current step injection was gradually increased by 25 pA steps until the target neuron fired the first spike, i.e. the threshold spike. This current level was determined as the threshold current of the neuron. Threshold spike amplitude was calculated as the voltage difference between the resting membrane potential and the peak of the threshold spike. Spike adaptation index of the responses to 100 and 400 Hz trains were calculated as the ratio between the firing rate during the last 5 seconds of the train and the firing rate during the first second of the train. Vector strength (Goldberg & Brown, 1969) of the stimulus train-evoked spikes was calculated using the formula: $\mathrm{VS} = \sqrt{(\Sigma sin\theta i)^2 + (\Sigma cos\theta i)^2}/n$, where θ_i is the phase angle of the spike i relative to the stimulation cycle, and n is the total number of spikes throughout the stimulus trains (Xie & Manis, 2013). Rayleigh statistics was calculated as $2n(VS)^2$. Neurons with $2n(VS)^2$ larger than 13.8 were considered to fire phase-locked spikes ($p <$

0.001) (Buunen & Rhode, 1978; Lu & Wang, 2000). Neurons with n less than 30, or fired less than 5 spikes per stimulus train were excluded from VS analysis. Spike jitter was calculated as the standard deviation of the spike latency relative to the stimulus onset.

Experimental design and statistical analysis

The study was cross-sectional using three different age groups of mice. The first set of study was conducted in young mice to characterize features of AN central synapses under normal hearing. Changes of AN synapses and postsynaptic neurons during hearing loss were further investigated in middle-aged and old mice groups with moderate and prominent ARHL, respectively. Statistical analysis used GraphPad Prism (version 6.0h). Kolmogorov-Smirnov test was first performed to examine whether population data were normally distributed. For data with normal distribution, unpaired t-test or one-way ANOVA followed by Tukey's multiple comparisons test was used as stated. For data that were not normally distributed, Mann Whitney test or Kruskal-Wallis test followed by Dunn's multiple comparisons test was used. Two-way ANOVA was performed to analyze the population data variances with calculated main effects of each of the factors and their interactions. All data were presented as mean ± SD except in Fig. 1C, which used mean ± SEM for clarity purpose of the panel.

RESULTS

CBA/CaJ mice and ARHL

Experiments in this study used CBA/CaJ mice, which developed progressive ARHL as shown by elevated hearing threshold and reduced wave I amplitude in ABRs to clicks (Fig. 1A). On average, the click threshold was 28 ± 4 dB SPL in young mice (n = 32), 37 ± 4 dB SPL in middle-aged mice (n = 22), and 70 ± 10 dB SPL in old mice (n = 43) (Fig. 1B; Kruskal-Wallis test: $p < 0.0001$; Dunn's multiple comparisons test: young vs. middle-aged, $p < 0.01$; young vs. old, $p < 0.0001$; middle-aged vs. old, $p < 0.0001$). With increasing sound intensity, the growth curve of the wave I amplitude became considerably flatter in middle-aged and old mice with significantly decreased peak amplitude (Fig. 1C; Two-way ANOVA: age effect, $F_{(2, 1477)} = 3309$, $p < 0.0001$; intensity effect, $F_{(13, 1477)} = 318$, $p < 0.0001$; interaction, $F_{(26, 1477)} = 121$, $p < 0.0001$). In particular, middle-aged mice showed relatively normal ABR threshold but greatly reduced ABR wave I amplitude, which resembles hidden hearing loss. The observed hearing profile is consistent with previous reports about CBA/CaJ mice (Sergeyenko *et al.*, 2013).

Different subtypes of AN central synapses converge onto individual CN neurons

Bushy neurons are the principal neurons of the AVCN that receives AN inputs via large endbulb of Held synapses on the soma (Manis *et al.*, 2011). We combined electrophysiology with post-hoc immunohistochemistry to identify the subtype-specificity of the AN synaptic inputs onto individual bushy neurons in parasagittal CN slices. Whole-cell current clamp recording was performed from target bushy neurons, which were filled with Alexa Fluor 594 included in the electrode solution (Fig. 2A–B). Slices were post-hoc immunostained using antibodies against VGluT1, which labels glutamate vesicles in all AN synaptic terminals, and calretinin, which labels only the AN fibers and synapses from type I_a SGNs (Materials and Methods). As shown in Fig. 2C, the bushy neuron received inputs from a large type I_a

endbulb of Held synapse (asterisk), which contained glutamate vesicles revealed by VGluT1-staining (arrow). In addition, there were VGluT1-labeled puncta (arrowhead) that were not enclosed in calretinin-labeled synapses, indicating that they were from non-type I_a AN synapses (presumably type I_b or I_c). Z-stack images were acquired to reconstruct the 3-dimentional structure of the type I_a endbulbs as well as VGluT1-labeled puncta surrounding the soma of the labeled bushy neuron (Fig. 2D–H; Supplemental Video 1). Using this approach, we show that type I_a and non-type I_a AN synapses converge onto individual CN bushy neurons (Fig. 2F).

The proportion of type I_a synaptic inputs correlates with physiological properties of postsynaptic neurons.

We studied the innervation patterns of type I_a and non-type I_a AN synapses onto 49 bushy neurons in normal hearing young mice as well as their electrophysiological response properties. Across the population, bushy neurons received different convergence of inputs from type I_a and non-type I_a synapses as shown in Fig. 3A, D, G, and J by different colors of VGluT1-labeled puncta. We measured the puncta volume and quantified the proportion of type I_a inputs (type I_a volume %) onto each bushy neuron, which varied on a continuum between those that received type I_a-dominant (I_a-D; with I_a volume > 50%; Fig. 3A, D) inputs and those with non-type I_a-dominant (Non-I_a-D; with I_a volume < 50%; Fig. 3G, J) inputs (Fig. 3M). The results suggest that auditory information from different subtypes of SGNs is systematically reassembled and processed in target CN neurons with gradually changing synaptic convergence. Interestingly, there was a significant correlation between the total volume of VGluT1-labeled puncta and the proportion of type I_a puncta volume (Fig. 3M), which indicates that neurons with higher proportion of type I_a inputs have larger volume of total VGluT1-labeled puncta, and thus stronger overall inputs from AN synapses.

To assess the intrinsic membrane properties of the target bushy neurons, we acquired electrophysiological responses to current step injections (Figure 2A–B; see Materials and Methods). Example responses from four bushy neurons in Fig. 3A, D, G, J are shown in Fig. 3B, E, H, K, respectively. Neurons with I_a-D inputs (Fig. 3B, E) had smaller threshold spike amplitude than those with Non-I_a-D inputs (Fig. 3H, K), which is shown by the negative correlation between threshold spike amplitude and the proportion of type I_a inputs among all bushy neurons (Fig. 3N). Compared to those with Non-I_a-D inputs, bushy neurons with I_a-D inputs showed significantly more depolarized resting membrane potential (Fig. 3P), smaller spike amplitude (Fig. 3R), required smaller current injection to trigger threshold spikes (Fig. 3S), but had similar input resistance (Fig. 3Q) (Table 1). The data suggests that bushy neurons with I_a-D inputs are more excitable than those with Non-I_a-D inputs.

We next investigated the AN evoked firing properties of target bushy neurons using responses to trains of AN stimulation (Fig. 2A–B). AN stimulation at 100 Hz evoked sustained spikes with moderate adaptation in neurons with I_a-D inputs (Fig. 3C, F), but only elicited transient or onset spikes in those with Non-I_a-D inputs (Fig. 3I, L). Spike adaptation index was calculated (see Materials and Methods) to quantify AN evoked firing patterns, in which higher adaptation index value corresponds to the firing of more sustained spikes and lower adaptation index value corresponds to the firing of transient/onset spikes. As shown in

Fig. 3O, there was a significant correlation between spike adaptation index and the proportion of type I_a inputs across all bushy neurons. In summary, neurons with I_a-D inputs showed significantly higher AN-evoked firing rate (Fig. 3T) and spike adaptation index (Fig. 3U) than neurons with Non-I_a-D inputs (Table 1). They also fired spikes with higher temporal precision, as revealed by significantly larger vector strength (Fig. 3V) and smaller spike jitter (Table 1).

AN can fire at sustained rates above 400 Hz under physiological conditions (Taberner & Liberman, 2005; Wen *et al.*, 2009). We further tested the firing properties of bushy neurons to high rate AN stimulation at 400 Hz (Fig. 4A–D). Similar to 100 Hz trains, 400 Hz AN stimulation evoked significantly higher firing rate (Fig. 4E) and spike adaptation index (Fig. 4F) in bushy neurons with I_a-D inputs than those with Non-I_a-D inputs (Table 1). No significant difference was found in the vector strength of evoked spikes (Fig. 4G) or spike jitter (Table 1). Most neurons (12 out of 21) with Non-I_a-D inputs fired insufficient number of spikes to 400 Hz stimulus trains and no vector strength or spike jitter were calculated from those neurons.

These results indicate that under normal hearing condition, AN synapses from different subtypes of SGNs innervate CN bushy neurons with systematically varying ratio of convergence, which correlates with distinct intrinsic property and AN evoked firing property of target neurons. The findings suggest a new dimension of neuronal organization within CN bushy cell population that dedicates to the reassembling and processing of auditory intensity information from different subtypes of SGNs.

AN synaptopathy and altered composition of bushy neuron population during ARHL

We next examined the innervation patterns of different AN synapses and the response properties of postsynaptic bushy neurons in middle-aged and old mice with different levels of ARHL (Fig. 1). Recordings were obtained from 31 bushy neurons (Figs. 5, 6) in middle-aged and 35 bushy neurons (Figs. 7, 8) in old mice.

Similar to those in young mice, we observed both bushy neurons with I_a-D inputs and those with Non-I_a-D inputs in middle-aged (Fig. 5A–M) and old (Fig. 7A–M) mice, except that the prevalence of neurons with Non-I_a-D inputs decreased with age (also see Fig. 9D and the discussion below). In general, the proportion of type I_a inputs remains correlated with the intrinsic and AN evoked response properties of the postsynaptic bushy neurons in both age groups with ARHL. Specifically, in middle-aged mice, higher proportion of type I_a inputs was correlated with smaller threshold spike amplitude (Fig. 5N), with target neurons tended to fire more sustained spikes (Fig. 5O). In summary, compared to those with Non-I_a-D inputs, bushy neurons with I_a-D inputs showed similar resting membrane potential (Fig. 5P) and input resistance (Fig. 5Q), but had significantly smaller threshold spike amplitude (Fig. 5R), were more excitable and required significantly smaller current injection to trigger threshold spikes (Fig. 5S) (Table 1).

In response to AN stimulus trains at 100 Hz, middle-aged neurons with I_a-D inputs showed a tendency to fire more spikes (Fig. 5T) with higher spike adaptation index (Fig. 5U; excluding 3 Non-I_a-D neurons that failed to fire any spike), as well as significantly better

temporal precision as revealed by larger vector strength (Fig. 5V) and smaller spike jitter (Table 1). In response to 400 Hz stimulus trains (Fig. 6A–D), bushy neurons from middle-aged mice showed similar differences between neurons with I_a-D inputs and those with Non-I_a-D inputs, in which the former fired at significantly higher rate (Fig. 6E) with higher spike adaptation index (Fig. 6F) (Table 1). No significant difference was found in their spike vector strength (Fig. 6G) or spike jitter (Table 1).

In old mice, higher proportion of type I_a inputs was also correlated with smaller threshold spike amplitude (Fig. 7N), with target neurons fired more sustained spikes (Fig. 7O). Compared to bushy neurons with Non-I_a-D inputs, neurons with I_a-D inputs showed similar resting membrane potential (Fig. 7P) and input resistance (Fig. 7Q), but had significantly smaller threshold spike amplitude (Fig. 7R) (Table 1). They had similar excitability with no significant difference in their threshold current level (Fig. 7S; Table 1). In response to AN stimulus trains at 100 Hz, neurons with I_a-D inputs fired significantly more spikes (Fig. 7T) with higher spike adaptation index (Fig. 7U) (Table 1). No significant difference was found in spike vector strength (Fig. 7V) or spike jitter (Table 1). In response to 400 Hz stimulus trains (Fig. 8A–D), bushy neurons with I_a-D inputs fired at significantly higher rate (Fig. 8E), but with similar spike adaptation index (Fig. 8F), vector strength (Fig. 8G) and spike jitter (Table 1).

To evaluate the morphological changes of AN synapses during ARHL, we compared the total volume as well as the volumes of subtype-specific VGluT1-labeled puncta in bushy neurons from mice of all three age groups. As shown in Fig. 9A, the total volume of VGluT1-labeled puncta in bushy neurons significantly decreased with age (young: 100 ± 50 μm^3, n = 49; middle-aged: 77 ± 31 μm^3, n = 31; old: 46 ± 25 μm^3, n = 35; one-way ANOVA: $F_{(2,112)} = 19.26$, $p < 0.0001$), suggesting an overall degeneration of AN synapses during ARHL. Further investigation of different AN subtypes showed that synaptic degeneration was significant in both type I_a synapses (Fig. 9B; type I_a VGluT1-labeled puncta, young: 61 ± 46 μm^3, n = 49; middle-aged: 52 ± 29 μm^3, n = 31; old: 36 ± 24 μm^3, n = 35; one-way ANOVA: $F_{(2,112)} = 5.00$, $p = 0.0083$) and non-type I_a synapses (Fig. 9C; Non-type I_a VGluT1-labeled puncta, young: 39 ± 31 μm^3, n = 49; middle-aged: 26 ± 17 μm^3, n = 31; old: 11 ± 9 μm^3, n = 35; Kruskal-Wallis test: $p < 0.0001$). Remarkably, the degeneration was more profound in non-type I_a synapses (Fig. 9B–C; two-way ANOVA: age effect, $F_{(2,224)} = 16.2$, $p < 0.0001$; synaptic subtype effect, $F_{(1,224)} = 36.2$, $p < 0.0001$; interaction, $F_{(2,224)} = 0.11$, $p = 0.900$). On average, the volume of VGluT1-labeled puncta from type I_a synapses decreased by 15% in middle-aged mice and 41% in old mice compared to young mice (Fig. 9B). In contrast, the volume of non-type I_a puncta decreased by 34% and 73% in middle-aged and old mice (Fig. 9C), respectively. These results indicate that there is a progressive AN central synaptopathy during aging, and this synaptopathy is biased toward being more severe in non-type I_a synapses.

Consistent with the more profound degeneration of non-type I_a synapses, the prevalence of postsynaptic bushy neurons with Non-I_a-D inputs progressively decreased with age (Fig. 9D; 49% in young, 26% in middle-aged, and 17% in old mice; also see Fig. 3M, 5M and 7M for the distribution of all individual neurons). Across different age groups, the differences between bushy neurons with I_a-D inputs and those with non-I_a-D inputs in both intrinsic

membrane properties (Fig. 9E–G) and AN-evoked firing responses (Fig. 9H–J) were retained. Specifically, bushy neurons with I_a-D inputs showed significantly depolarized resting membrane potential (Fig. 9E; two-way ANOVA: cell type effect, $F_{(1,109)} = 4.98$, p = 0.028; age effect, $F_{(2,109)} = 0.42$, p = 0.656; interaction, $F_{(2,109)} = 1.05$, p = 0.352), smaller threshold spike amplitude (Fig. 9F; two-way ANOVA: cell type effect, $F_{(1,109)} = 20.88$, p < 0.0001; age effect, $F_{(2,109)} = 0.17$, p = 0.841; interaction, $F_{(2,109)} = 0.39$, p = 0.678), were more excitable with smaller threshold current (Fig. 9G; two-way ANOVA: cell type effect, $F_{(1,109)} = 15.18$, p = 0.0002; age effect, $F_{(2,109)} = 1.16$, p = 0.319; interaction, $F_{(2,109)} = 0.44$, p = 0.648), fired more spikes to AN stimulation at 100 Hz (Fig. 9H; two-way ANOVA: cell type effect, $F_{(1,109)} = 15.55$, p = 0.0001; age effect, $F_{(2,109)} = 1.67$, p = 0.193; interaction, $F_{(2,109)} = 0.09$, p = 0.912) with higher spike adaptation index (Fig. 9I; two-way ANOVA: cell type effect, $F_{(1,94)} = 9.74$, p = 0.0024; age effect, $F_{(2,94)} = 1.61$, p = 0.205; interaction, $F_{(2,94)} = 0.35$, p = 0.702) and higher vector strength (Fig. 9J; two-way ANOVA: cell type effect, $F_{(1,88)} = 24.08$, p < 0.0001; age effect, $F_{(2,88)} = 8.60$, p = 0.0004; interaction, $F_{(2,88)} = 2.70$, p = 0.073). However, there were increasingly more neurons during aging that failed to fire any spike to AN stimulation (Fig. 5L, 7L) (3/49 in young, 5/31 in middle-aged, 7/35 in old mice). The results suggest an age-related shift in the composition of bushy neuron population during ARHL in the direction of having relatively more neurons with I_a-D inputs.

Endbulbs show decreased synaptic strength with age during ARHL

To evaluate the synaptic strength of the endbulb of Held onto bushy neurons during ARHL, we analyzed the evoked EPSPs that failed to trigger any spikes during the response to 100 Hz stimulus trains (Fig. 10). EPSPs that did trigger spikes were often merged with the spike waveform (Fig. 10A) and therefore excluded from this analysis. As shown in Fig. 10B, the average EPSP amplitude showed no difference overall between neurons with I_a-D and Non-I_a-D inputs, but was significantly decreased with age (two-way ANOVA: cell type effect, $F_{(1,94)} = 0.149$, $p = 0.701$; age effect, $F_{(2,94)} = 5.17$, $p = 0.0074$; interaction, $F_{(2,94)} = 0.163$, $p = 0.850$). We used two additional EPSP measurements to estimate the threshold of the synaptic inputs in triggering postsynaptic spikes. The first was EPSP amplitude at 90th percentile, which was significantly decreased with age (Fig. 10C; two-way ANOVA: cell type effect, $F_{(1,94)} = 0.117$, $p = 0.733$; age effect, $F_{(2,94)} = 3.82$, $p = 0.025$; interaction, $F_{(2,94)} = 0.163$, $p = 0.850$). As bushy neurons often exhibit a rate threshold of the membrane potential depolarization (McGinley & Oertel, 2006), we secondly calculated the maximum rising slope of each EPSP, which was determined as the peak of the first derivative during the EPSP rising phase (Fig. 10D) (Xie & Manis, 2013). The rate threshold was estimated to be the 90th percentile of the EPSP maximum slope in each bushy neuron, which was also significantly decreased with age (Fig. 10E; two-way ANOVA: cell type effect, $F_{(1,94)} = 2.73$, $p = 0.102$; age effect, $F_{(2,94)} = 5.11$, $p = 0.0078$; interaction, $F_{(2,94)} = 0.603$, $p = 0.549$). The results suggest that the synaptic strength at the endbulb of Held was weakened during aging, which is consistent with the overall degeneration of AN synapses (Fig. 9A–C). However, preferential reduction in synaptic strength of the Non-I_a-D inputs was not detected (Fig. 10B), possibly due to the small number of neurons with Non-I_a-D inputs in aged groups. The decreased threshold to AN synaptic input with age (Fig. 10C, E) may reflect

homeostatic changes of CN neurons that compensate the reduced sensory inputs from the AN during ARHL (Xie, 2016).

Synaptopathy in individual type I_a endbulb of Held synapses during ARHL

As calretinin-staining labels the entire type I_a synaptic terminal, we reconstructed the 3-dimensional profile of individual type I_a endbulb of Held synapses onto bushy neurons from three age groups of mice (Fig. 11A–C). Bushy neurons with identifiable type I_a endbulb terminals received between 1 – 3 type I_a endbulbs, with an average of 1.5 ± 0.6 (n = 64) in young, 1.5 ± 0.6 (n = 20) in middle-aged, and 1.7 ± 0.7 (n = 32) in old mice (Kruskal-Wallis test: $p = 0.472$). Individual type I_a endbulbs degenerated during aging with significantly decreased volume of the synaptic terminal (Fig. 11D; young: 218 ± 101 μm^3, n = 98; middle-aged: 126 ± 63 μm^3, n = 29; old: 104 ± 64 μm^3, n = 53; Kruskal-Wallis test: $p < 0.0001$) as well as the volume of VGluT1-labeled puncta within each endbulb (Fig. 11E; young: 70 ± 37 μm^3, n = 98; middle-aged: 35 ± 18 μm^3, n = 29; old: 29 ± 15 μm^3, n = 53; Kruskal-Wallis test: $p < 0.0001$). However, there was no change in the volume ratio between the two (Fig. 11F; young: 0.32 ± 0.11, n = 98; middle-aged: 0.29 ± 0.10, n = 29; old: 0.30 ± 0.11, n = 53; Kruskal-Wallis test: $p = 0.416$), suggesting that the relative quantity of synaptic vesicles within given synaptic terminal space remains unchanged during aging. Thus, AN synaptopathy during ARHL occurs with reduced synaptic terminal volume as well as a balanced decrease in the functional components of the synaptic machinery, at least in type I_a endbulb of Held synapses.

DISCUSSION

Convergence of AN synaptic inputs onto individual CN neurons and intensity processing

Information about sound intensity from each inner hair cell is conveyed by distributed firing rates amongst three subtypes of type I SGNs that operate over different ranges (Liberman, 1978). How this information is reassembled in CN neurons for central processing has remained unclear despite decades of research. Classical studies relied on tracing individual HRP filled AN fibers with known spontaneous rates (Fekete *et al.*, 1984; Sento & Ryugo, 1989; Liberman, 1991; Ryugo & Sento, 1991; Liberman, 1993; Ryugo *et al.*, 1996; Tsuji & Liberman, 1997; Ryugo, 2008). Because most filled AN fibers ended on different cells, it was not clear how different subtypes of AN synapses converge onto individual CN neurons. The physiological properties of these postsynaptic neurons were also unknown. Recent identification of molecular markers for different subtypes of type I SGNs (Petitpre *et al.*, 2018; Shrestha *et al.*, 2018; Sun *et al.*, 2018) made this study possible. In particular, we used calretinin as the marker to differentiate AN central synapses of type I_a SGNs from those of other non-type I_a SGN subtypes. It remains a challenge to identify type I_b and I_c AN central synapses, which were collectively analyzed as non-calretinin-expressing (non-type I_a) synapses in this study.

Sharma et al (2018) showed that calretinin-expressing SGNs synapse onto inner hair cells on the pillar side and non-calretinin-expressing SGNs synapse on the modiolar side, which respectively correspond to the SGN subtype with high spontaneous rate/low threshold and those with medium/low spontaneous rate and medium/high threshold (Liberman, 1978,

1982b). Therefore, our findings about the innervation pattern of calretinin-expressing and non-calretinin-expressing endbulbs onto CN bushy neurons suggest that sound intensity information from different subtypes of SGNs is systematically transformed and processed in the central auditory system in a new dimension that extends even within a traditionally classified cell type. In this case, CN bushy neurons have been long recognized as a specialized cell population in the CN that dedicates to the processing of information about the temporal fine structure of sound (Joris *et al.*, 1994a; Joris *et al.*, 1994b; Manis *et al.*, 2011). Our findings showed that within this bushy neuron population, cells differentiate physiologically based on the subtype composition of their AN synaptic inputs, i.e. the relative amount of information they receive about different sound intensities. Specifically, neurons with I_a-D inputs preferentially process information about low intensity sound, are more excitable and can fire sustained spikes to prolonged AN inputs (optimal for encoding persistent sound); while neurons with Non-I_a-D inputs are devoted to process information about medium and high intensity sound, are less excitable and only fire transiently to prolonged AN inputs (optimal for detecting loud auditory transients). It is worth noting that we did not classify our recorded bushy cells into the traditional spherical and globular bushy cell types, as it is difficult to unambiguously identify these neurons in mice (Lauer *et al.*, 2013). It is unclear if spherical and globular bushy neurons indeed receive different convergence of inputs from type I_a and non-type I_a AN synapses.

Cochlear synaptopathy and AN central synaptopathy

Cochlear synaptopathy has been a research focus in recent years (Kujawa & Liberman, 2015; Liberman, 2017), which characterizes the anatomical loss of SGN peripheral synapses under pathological conditions. Due to the small size, it is hard to investigate whether the surviving cochlear synapses retain normal physiological function or are functionally compromised after damage. In this study, we characterized AN central synaptopathy from a different perspective. While we could not investigate the lost AN central synapses, we were able to elucidate the pathological changes of the surviving AN central synapses both physiologically using whole-cell recording and anatomically using post-hoc immunohistochemistry on the recorded neurons. As most cochlear synapses and SGNs (> 70%) survive during normal aging (Sergeyenko *et al.*, 2013), it is of significant importance to understand the physiological changes of the existing synapses, whose function is critical in supporting the remaining auditory system and therefore the residual hearing of the subject. Indeed, our findings on AN central synaptopathy showed that the surviving synapses degenerate both anatomically and physiologically during aging, and may play significant roles in the development of ARHL.

AN synaptopathy and altered CN neuronal composition during ARHL

The observed AN central synaptopathy could be the consequence of aging at the synapse, as aging universally impacts every structure. In this case, however, it is hard to justify the preferential degeneration of non-type I_a synapses in ARHL groups. Therefore, AN central synaptopathy are likely secondary changes after primary damages of SGNs at the peripheral synapses, which lead to diminished physiological activity as well as loss of SGNs following long-term delay (Furman *et al.*, 2013; Sergeyenko *et al.*, 2013; Kujawa & Liberman, 2015; Liberman, 2017). The decrease in VGluT1-labeled puncta per bushy neuron (Fig. 9A–C)

probably reflects both the degeneration of central synapses from the surviving SGNs (Fig. 10) as well as the loss of entire central synapses from lost SGNs. Given that low spontaneous rate/high threshold (type I_c) SGNs are preferentially damaged under pathological conditions (Furman *et al.*, 2013; Shrestha *et al.*, 2018), it is not surprising that central synaptopathy is more severe in non-type I_a AN synapses during ARHL. Such biased AN synaptopathy consequently results in relatively more abundant type I_a synapses among the surviving population.

ARHL is also associated with changes throughout the central auditory system (Frisina & Walton, 2006; Caspary *et al.*, 2008; Profant *et al.*, 2013; Groschel *et al.*, 2014; Ouda *et al.*, 2015), particularly the compromised ability in processing sound information during auditory tasks (Lorenzi *et al.*, 2006; Grose & Mamo, 2010; Anderson *et al.*, 2012; Atcherson *et al.*, 2015). The link between cochlear pathology and central auditory processing deficits during ARHL remains unclear. For the first time, we show in this study that AN central synaptopathy, which presumably links to cochlear pathology, is associated with significant changes in the CN that include shifted neuronal composition of bushy neurons. It is conceivable that such changes alter the physiological responses across the CN neuronal population and the overall representation of auditory information. Since CN neurons initiate parallel pathways in the central auditory system (Cant & Benson, 2003), the shifted composition of CN neuronal population could be the trigger of many central auditory processing disorders including hyperacusis (loudness intolerance) and tinnitus (Vogler *et al.*, 2011; Wang *et al.*, 2011; Niu *et al.*, 2013; Caspary & Llano, 2017; Luo *et al.*, 2017; Radziwon *et al.*, 2019; Sheppard *et al.*, 2019; Shore & Wu, 2019). Further investigation of the synaptic and cellular changes of the CN is essential in understanding the relationship between cochlear pathology and central auditory processing disorders under different hearing impairment conditions.

Remarkably, CBA/CaJ mice in the middle-aged group had relatively normal ABR threshold but greatly reduced wave I amplitude (Fig. 1), a scenario that mimics hidden hearing loss (Sergeyenko *et al.*, 2013; Kujawa & Liberman, 2015). Both biased AN synaptopathy (Fig. 9A–C) and shifted composition of neuronal population (Fig. 9D) were profound in this age group. The findings suggest that in addition to selective cochlear synaptopathy (Kujawa & Liberman, 2015), which is considered the primary cause of hidden hearing loss, significant changes also occur in central structure along the auditory pathway before hearing loss becomes substantial. In this case, decreased prevalence of bushy neurons with Non-I_a-D inputs (Fig. 9D) in middle-aged mice suggests that temporal processing of middle/high intensity sound from non-type I_a SGNs is compromised in CN neural circuitry and probably also in connected higher nuclei of the auditory system.

Response properties of CN bushy neurons during ARHL

CN bushy neurons were previously shown to vary in intrinsic membrane properties due to different composition of voltage gated ion channels (Manis & Marx, 1991; Rothman & Manis, 2003; Cao *et al.*, 2007; Manis *et al.*, 2019). We found in this study that the intrinsic membrane property as well as the AN evoked firing property of bushy neurons correlate with the proportion of type I_a synapses they receive, which suggests that bushy neurons are

each optimized with a unique combination of anatomical and physiological features to process the distinctively converged auditory information from different SGNs. In young mice with normal hearing, bushy neurons showed a continuous ratio of distribution in the proportion of type I_a synaptic inputs they receive (Fig. 3M) as well as their physiological properties (Fig. 3N–O). The distribution became bimodal during ARHL, especially in the old mice group (Fig. 7M–O), presumably due to the preferential synaptopathy of non-type I_a synapses. We hence classified bushy neurons into two subgroups, including neurons with I_a-D inputs and those with Non-I_a-D inputs. Despite the changed neuronal prevalence (Fig. 9D), the physiological properties of two bushy neuron subpopulations remain distinct in all age groups during ARHL (Fig. 9E–J), suggesting that the function of CN bushy neurons are tightly regulated by the types of AN inputs they receive. It remains unclear whether the altered bushy neuron prevalence during ARHL is due to the loss of bushy neurons with Non-I_a-D inputs after biased AN synaptopathy, or the conversion of neurons with Non-I_a-D inputs to those with I_a-D inputs after adaptive changes like altered expression of voltage-gated ion channels.

Clinical implications

Cochlear implantation has been widely used in the clinic to treat profound hearing loss. Its performance relies on the function of SGNs, especially the SGN central structure. Age-related AN central synaptopathy is no doubt one of the key factors that limit the performance of cochlear implants. Indeed, duration of deafness is the most important predictor of the post implant outcomes (Rubinstein *et al.*, 1999). The stimulation parameters of modern cochlear implants presumably activate all SGNs indiscriminately. This study suggests that, if possible, differential stimulation of different subtypes of SGNs in cochlear implants with enhanced activation of non-type I_a SGNs may compensate the biased AN central synaptopathy and altered CN neural circuitry, which would enhance compromised auditory processing, improve cochlear implant performance and overall hearing.

Supplementary Material

Refer to Web version on PubMed Central for supplementary material.

Acknowledgements

This work was supported by NIH grant R01DC016037 to R.X.. Images and video were generated at OSU Campus Microscopy and Imaging Facility, supported by grant P30CA016058. We thank Paul B. Manis for comments on the manuscript.

References

Anderson S, Parbery-Clark A, White-Schwoch T & Kraus N. (2012). Aging affects neural precision of speech encoding. J Neurosci 32, 14156–14164. [PubMed: 23055485]

Atcherson SR, Nagaraj NK, Kennett SE & Levisee M. (2015). Overview of Central Auditory Processing Deficits in Older Adults. Semin Hear 36, 150–161. [PubMed: 27516715]

Buunen TJ & Rhode WS. (1978). Responses of fibers in the cat's auditory nerve to the cubic difference tone. The Journal of the Acoustical Society of America 64, 772–781. [PubMed: 701616]

Cant NB & Benson CG. (2003). Parallel auditory pathways: projection patterns of the different neuronal populations in the dorsal and ventral cochlear nuclei. Brain research bulletin 60, 457–474. [PubMed: 12787867]

Cant NB & Morest DK. (1979). Organization of the neurons in the anterior division of the anteroventral cochlear nucleus of the cat. Light-microscopic observations. Neuroscience 4, 1909–1923. [PubMed: 530438]

Cao XJ, Shatadal S & Oertel D. (2007). Voltage-sensitive conductances of bushy cells of the Mammalian ventral cochlear nucleus. J Neurophysiol 97, 3961–3975. [PubMed: 17428908]

Caspary DM, Ling L, Turner JG & Hughes LF. (2008). Inhibitory neurotransmission, plasticity and aging in the mammalian central auditory system. J Exp Biol 211, 1781–1791. [PubMed: 18490394]

Caspary DM & Llano DA. (2017). Auditory thalamic circuits and GABAA receptor function: Putative mechanisms in tinnitus pathology. Hear Res 349, 197–207. [PubMed: 27553899]

Fekete DM, Rouiller EM, Liberman MC & Ryugo DK. (1984). The central projections of intracellularly labeled auditory nerve fibers in cats. J Comp Neurol 229, 432–450. [PubMed: 6209306]

Frisina RD & Walton JP. (2006). Age-related structural and functional changes in the cochlear nucleus. Hear Res 216–217, 216–223.

Furman AC, Kujawa SG & Liberman MC. (2013). Noise-induced cochlear neuropathy is selective for fibers with low spontaneous rates. J Neurophysiol 110, 577–586. [PubMed: 23596328]

Goldberg JM & Brown PB. (1969). Response of binaural neurons of dog superior olivary complex to dichotic tonal stimuli: some physiological mechanisms of sound localization. J Neurophysiol 32, 613–636. [PubMed: 5810617]

Groschel M, Hubert N, Muller S, Ernst A & Basta D. (2014). Age-dependent changes of calcium related activity in the central auditory pathway. Exp Gerontol 58, 235–243. [PubMed: 25176163]

Grose JH & Mamo SK. (2010). Processing of temporal fine structure as a function of age. Ear and hearing 31, 755–760. [PubMed: 20592614]

Joris PX, Carney LH, Smith PH & Yin TC. (1994a). Enhancement of neural synchronization in the anteroventral cochlear nucleus. I. Responses to tones at the characteristic frequency. J Neurophysiol 71, 1022–1036. [PubMed: 8201399]

Joris PX, Smith PH & Yin TC. (1994b). Enhancement of neural synchronization in the anteroventral cochlear nucleus. II. Responses in the tuning curve tail. J Neurophysiol 71, 1037–1051. [PubMed: 8201400]

Karadottir R & Attwell D. (2006). Combining patch-clamping of cells in brain slices with immunocytochemical labeling to define cell type and developmental stage. Nat Protoc 1, 1977–1986. [PubMed: 17487186]

Kiang NY, Rho JM, Northrop CC, Liberman MC & Ryugo DK. (1982). Hair-cell innervation by spiral ganglion cells in adult cats. Science 217, 175–177. [PubMed: 7089553]

Kujawa SG & Liberman MC. (2015). Synaptopathy in the noise-exposed and aging cochlea: Primary neural degeneration in acquired sensorineural hearing loss. Hear Res 330, 191–199. [PubMed: 25769437]

Lauer AM, Connelly CJ, Graham H & Ryugo DK. (2013). Morphological Characterization of Bushy Cells and Their Inputs in the Laboratory Mouse (Mus musculus) Anteroventral Cochlear Nucleus. PLoS One 8, e73308. [PubMed: 23991186]

Liberman LD, Suzuki J & Liberman MC. (2015). Dynamics of cochlear synaptopathy after acoustic overexposure. J Assoc Res Otolaryngol 16, 205–219. [PubMed: 25676132]

Liberman MC. (1978). Auditory-nerve response from cats raised in a low-noise chamber. The Journal of the Acoustical Society of America 63, 442–455. [PubMed: 670542]

Liberman MC. (1980). Morphological differences among radial afferent fibers in the cat cochlea: an electron-microscopic study of serial sections. Hear Res 3, 45–63. [PubMed: 7400048]

Liberman MC. (1982a). The cochlear frequency map for the cat: labeling auditory-nerve fibers of known characteristic frequency. The Journal of the Acoustical Society of America 72, 1441–1449. [PubMed: 7175031]

Liberman MC. (1982b). Single-neuron labeling in the cat auditory nerve. Science 216, 1239–1241. [PubMed: 7079757]

Liberman MC. (1991). Central projections of auditory-nerve fibers of differing spontaneous rate. I. Anteroventral cochlear nucleus. J Comp Neurol 313, 240–258. [PubMed: 1722487]

Liberman MC. (1993). Central projections of auditory nerve fibers of differing spontaneous rate, II: Posteroventral and dorsal cochlear nuclei. J Comp Neurol 327, 17–36. [PubMed: 8432906]

Liberman MC. (2017). Noise-induced and age-related hearing loss: new perspectives and potential therapies. F1000Res 6, 927. [PubMed: 28690836]

Liberman MC & Oliver ME. (1984). Morphometry of intracellularly labeled neurons of the auditory nerve: correlations with functional properties. J Comp Neurol 223, 163–176. [PubMed: 6200517]

Lin S & Xie R. (2019). Principal Neurons in the Anteroventral Cochlear Nucleus Express Cell-Type Specific Glycine Receptor alpha Subunits. Neuroscience 415, 77–88. [PubMed: 31325562]

Lorenzi C, Gilbert G, Carn H, Garnier S & Moore BC. (2006). Speech perception problems of the hearing impaired reflect inability to use temporal fine structure. Proc Natl Acad Sci U S A 103, 18866–18869. [PubMed: 17116863]

Lu T & Wang X. (2000). Temporal discharge patterns evoked by rapid sequences of wide- and narrowband clicks in the primary auditory cortex of cat. J Neurophysiol 84, 236–246. [PubMed: 10899199]

Luo H, Pace E & Zhang J. (2017). Blast-induced tinnitus and hyperactivity in the auditory cortex of rats. Neuroscience 340, 515–520. [PubMed: 27865868]

Manis PB, Kasten MR & Xie R. (2019). Classification of neurons in the adult mouse cochlear nucleus: Linear discriminant analysis. PLoS One 14, e0223137. [PubMed: 31581200]

Manis PB & Marx SO. (1991). Outward currents in isolated ventral cochlear nucleus neurons. J Neurosci 11, 2865–2880. [PubMed: 1880553]

Manis PB, Xie R, Wang Y, Marrs GS & Spirou GA. (2011). The Endbulbs of Held. In Synaptic Mechanisms in the Auditory System, ed. Trussell LO, Popper AN & Fay RR, pp. 61–93. Springer, New York.

McGinley MJ & Oertel D. (2006). Rate thresholds determine the precision of temporal integration in principal cells of the ventral cochlear nucleus. Hear Res 216–217, 52–63.

Moore BC. (2008). The role of temporal fine structure processing in pitch perception, masking, and speech perception for normal-hearing and hearing-impaired people. J Assoc Res Otolaryngol 9, 399–406. [PubMed: 18855069]

Nayagam BA, Muniak MA & Ryugo DK. (2011). The spiral ganglion: connecting the peripheral and central auditory systems. Hear Res 278, 2–20. [PubMed: 21530629]

Niu Y, Kumaraguru A, Wang R & Sun W. (2013). Hyperexcitability of inferior colliculus neurons caused by acute noise exposure. J Neurosci Res 91, 292–299. [PubMed: 23151900]

Oleskevich S & Walmsley B. (2002). Synaptic transmission in the auditory brainstem of normal and congenitally deaf mice. J Physiol 540, 447–455. [PubMed: 11956335]

Ouda L, Profant O & Syka J. (2015). Age-related changes in the central auditory system. Cell and tissue research 361, 337–358. [PubMed: 25630878]

Parthasarathy A & Kujawa SG. (2018). Synaptopathy in the Aging Cochlea: Characterizing Early-Neural Deficits in Auditory Temporal Envelope Processing. J Neurosci 38, 7108–7119. [PubMed: 29976623]

Petitpre C, Wu H, Sharma A, Tokarska A, Fontanet P, Wang Y, Helmbacher F, Yackle K, Silberberg G, Hadjab S & Lallemend F. (2018). Neuronal heterogeneity and stereotyped connectivity in the auditory afferent system. Nature communications 9, 3691.

Profant O, Balogova Z, Dezortova M, Wagnerova D, Hajek M & Syka J. (2013). Metabolic changes in the auditory cortex in presbycusis demonstrated by MR spectroscopy. Exp Gerontol 48, 795–800. [PubMed: 23648586]

Radziwon K, Auerbach BD, Ding D, Liu X, Chen GD & Salvi R. (2019). Noise-Induced loudness recruitment and hyperacusis: Insufficient central gain in auditory cortex and amygdala. Neuroscience 422, 212–227. [PubMed: 31669363]

Rothman JS & Manis PB. (2003). Differential expression of three distinct potassium currents in the ventral cochlear nucleus. J Neurophysiol 89, 3070–3082. [PubMed: 12783951]

Rouiller EM, Cronin-Schreiber R, Fekete DM & Ryugo DK. (1986). The central projections of intracellularly labeled auditory nerve fibers in cats: an analysis of terminal morphology. J Comp Neurol 249, 261–278. [PubMed: 3734159]

Rubinstein JT, Parkinson WS, Tyler RS & Gantz BJ. (1999). Residual speech recognition and cochlear implant performance: effects of implantation criteria. Am J Otol 20, 445–452. [PubMed: 10431885]

Ryugo DK. (2008). Projections of low spontaneous rate, high threshold auditory nerve fibers to the small cell cap of the cochlear nucleus in cats. Neuroscience 154, 114–126. [PubMed: 18155852]

Ryugo DK & Fekete DM. (1982). Morphology of primary axosomatic endings in the anteroventral cochlear nucleus of the cat: a study of the endbulbs of Held. J Comp Neurol 210, 239–257. [PubMed: 7142440]

Ryugo DK, Pongstaporn T, Huchton DM & Niparko JK. (1997). Ultrastructural analysis of primary endings in deaf white cats: morphologic alterations in endbulbs of Held. J Comp Neurol 385, 230–244. [PubMed: 9268125]

Ryugo DK, Rosenbaum BT, Kim PJ, Niparko JK & Saada AA. (1998). Single unit recordings in the auditory nerve of congenitally deaf white cats: morphological correlates in the cochlea and cochlear nucleus. J Comp Neurol 397, 532–548. [PubMed: 9699914]

Ryugo DK & Sento S. (1991). Synaptic connections of the auditory nerve in cats: relationship between endbulbs of held and spherical bushy cells. J Comp Neurol 305, 35–48. [PubMed: 2033123]

Ryugo DK, Wu MM & Pongstaporn T. (1996). Activity-related features of synapse morphology: a study of endbulbs of held. J Comp Neurol 365, 141–158. [PubMed: 8821447]

Sento S & Ryugo DK. (1989). Endbulbs of held and spherical bushy cells in cats: morphological correlates with physiological properties. J Comp Neurol 280, 553–562. [PubMed: 2708566]

Sergeyenko Y, Lall K, Liberman MC & Kujawa SG. (2013). Age-related cochlear synaptopathy: an early-onset contributor to auditory functional decline. J Neurosci 33, 13686–13694. [PubMed: 23966690]

Shannon RV, Zeng FG, Kamath V, Wygonski J & Ekelid M. (1995). Speech recognition with primarily temporal cues. Science 270, 303–304. [PubMed: 7569981]

Sharma K, Seo YW & Yi E. (2018). Differential Expression of Ca(2+)-buffering Protein Calretinin in Cochlear Afferent Fibers: A Possible Link to Vulnerability to Traumatic Noise. Exp Neurobiol 27, 397–407. [PubMed: 30429649]

Sheppard A, Liu X, Alkharabsheh A, Chen GD & Salvi R. (2019). Intermittent Low-level Noise Causes Negative Neural Gain in the Inferior Colliculus. Neuroscience 407, 135–145. [PubMed: 30458217]

Shore SE & Wu C. (2019). Mechanisms of Noise-Induced Tinnitus: Insights from Cellular Studies. Neuron 103, 8–20. [PubMed: 31271756]

Shrestha BR, Chia C, Wu L, Kujawa SG, Liberman MC & Goodrich LV. (2018). Sensory Neuron Diversity in the Inner Ear Is Shaped by Activity. Cell 174, 1229–1246 e1217. [PubMed: 30078709]

Spirou GA, Rager J & Manis PB. (2005). Convergence of auditory-nerve fiber projections onto globular bushy cells. Neuroscience 136, 843–863. [PubMed: 16344156]

Spoendlin H (1969). Innervation patterns in the organ of corti of the cat. Acta Otolaryngol 67, 239–254. [PubMed: 5374642]

Sun S, Babola T, Pregernig G, So KS, Nguyen M, Su SM, Palermo AT, Bergles DE, Burns JC & Muller U. (2018). Hair Cell Mechanotransduction Regulates Spontaneous Activity and Spiral Ganglion Subtype Specification in the Auditory System. Cell 174, 1247–1263 e1215. [PubMed: 30078710]

Taberner AM & Liberman MC. (2005). Response properties of single auditory nerve fibers in the mouse. J Neurophysiol 93, 557–569. [PubMed: 15456804]

Tsuji J & Liberman MC. (1997). Intracellular labeling of auditory nerve fibers in guinea pig: central and peripheral projections. J Comp Neurol 381, 188–202. [PubMed: 9130668]

Vogler DP, Robertson D & Mulders WH. (2011). Hyperactivity in the ventral cochlear nucleus after cochlear trauma. J Neurosci 31, 6639–6645. [PubMed: 21543592]

Wang H, Brozoski TJ & Caspary DM. (2011). Inhibitory neurotransmission in animal models of tinnitus: maladaptive plasticity. Hear Res 279, 111–117. [PubMed: 21527325]

Wang Y & Manis PB. (2005). Synaptic transmission at the cochlear nucleus endbulb synapse during age-related hearing loss in mice. J Neurophysiol 94, 1814–1824. [PubMed: 15901757]

Wang Y, Wang M & Xie R. (2019). D-Stellate Neurons of the Ventral Cochlear Nucleus Decrease in Auditory Nerve-Evoked Activity during Age-Related Hearing Loss. Brain Sci 9.

Webster DB & Trune DR. (1982). Cochlear nuclear complex of mice. Am J Anat 163, 103–130. [PubMed: 7072613]

Wen B, Wang GI, Dean I & Delgutte B. (2009). Dynamic range adaptation to sound level statistics in the auditory nerve. J Neurosci 29, 13797–13808. [PubMed: 19889991]

Wright S, Hwang Y & Oertel D. (2014). Synaptic transmission between end bulbs of Held and bushy cells in the cochlear nucleus of mice with a mutation in Otoferlin. J Neurophysiol 112, 3173–3188. [PubMed: 25253474]

Wu SH & Oertel D. (1984). Intracellular injection with horseradish peroxidase of physiologically characterized stellate and bushy cells in slices of mouse anteroventral cochlear nucleus. J Neurosci 4, 1577–1588. [PubMed: 6726347]

Xie R (2016). Transmission of auditory sensory information decreases in rate and temporal precision at the endbulb of Held synapse during age-related hearing loss. J Neurophysiol 116, 2695–2705. [PubMed: 27683884]

Xie R & Manis PB. (2013). Target-specific IPSC kinetics promote temporal processing in auditory parallel pathways. J Neurosci 33, 1598–1614. [PubMed: 23345233]

Xie R & Manis PB. (2017a). Radiate and planar multipolar neurons of the mouse anteroventral cochlear nucleus: Intrinsic excitability and characterization of their auditory nerve input. Frontiers in neural circuits.

Xie R & Manis PB. (2017b). Synaptic transmission at the endbulb of Held deteriorates during age-related hearing loss. J Physiol 595, 919–934. [PubMed: 27618790]

Yu WM & Goodrich LV. (2014). Morphological and physiological development of auditory synapses. Hear Res 311, 3–16. [PubMed: 24508369]

Zhuang X, Sun W & Xu-Friedman MA. (2017). Changes in Properties of Auditory Nerve Synapses following Conductive Hearing Loss. J Neurosci 37, 323–332. [PubMed: 28077712]

KEY POINTS SUMMARY

- Sound information is transmitted by different subtypes of SGNs from the ear to the brain.
- Selective damage of SGN peripheral synapses (cochlear synaptopathy) is widely recognized as one of the primary mechanisms of hearing loss, while the mechanisms at the SGN central synapses remain unclear.
- We report that different subtypes of SGN central synapses converge at different ratios onto individual target CN neurons with distinct physiological properties, and show biased morphological and physiological changes during ARHL.
- The results reveal a new dimension in CN neural circuitry that systematically reassembles and processes auditory information from different SGN subtypes, which is altered during aging and likely contributes to the development of ARHL.
- In addition to known cochlear synaptopathy, this study shows that SGN central synapses are also pathologically changed during aging, which collectively help us better understand the structure and function of SGNs during ARHL.

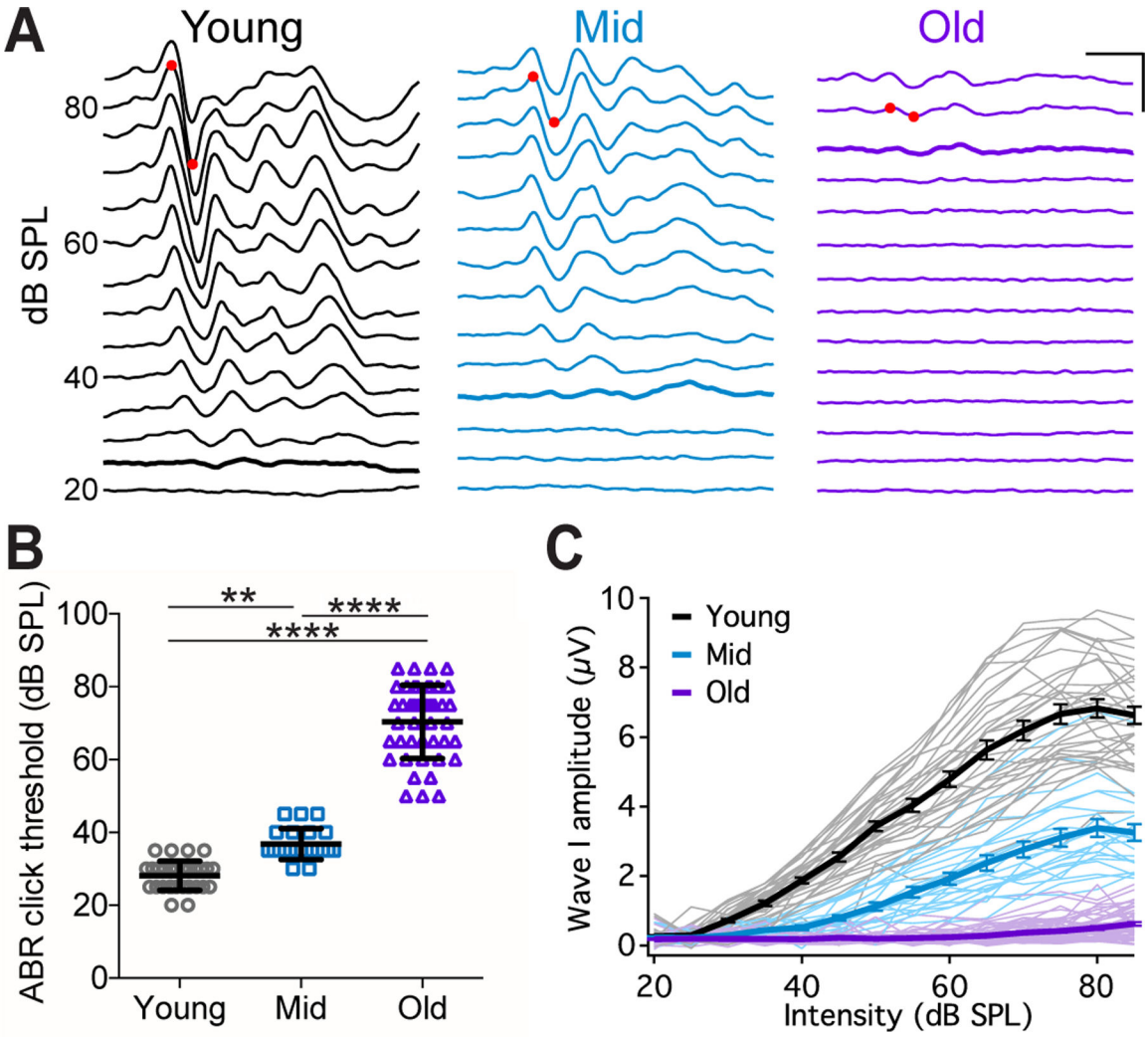

Figure 1. CBA/CaJ mice show age-related hearing loss (ARHL)

(**A**) Example ABR waveforms from mice at different ages to clicks at different intensities. Red dots mark the positive and negative peaks of ABR wave I at 80 dB SPL. Thick traces: ABR threshold trace. Scale: 2 ms, 5 μV.

(**B**) ABR click thresholds in 32 young, 22 middle-aged, and 43 old mice. Dunn's multiple comparisons test: **$p < 0.001$; ****$p < 0.0001$. ABR threshold was beyond 85 dB SPL in 12 old mice and not determined.

(**C**) Growth curves of ABR wave I amplitude in all mice. Thin lines: individual mice; thick lines: average of each age group, with error bars represent SEM.

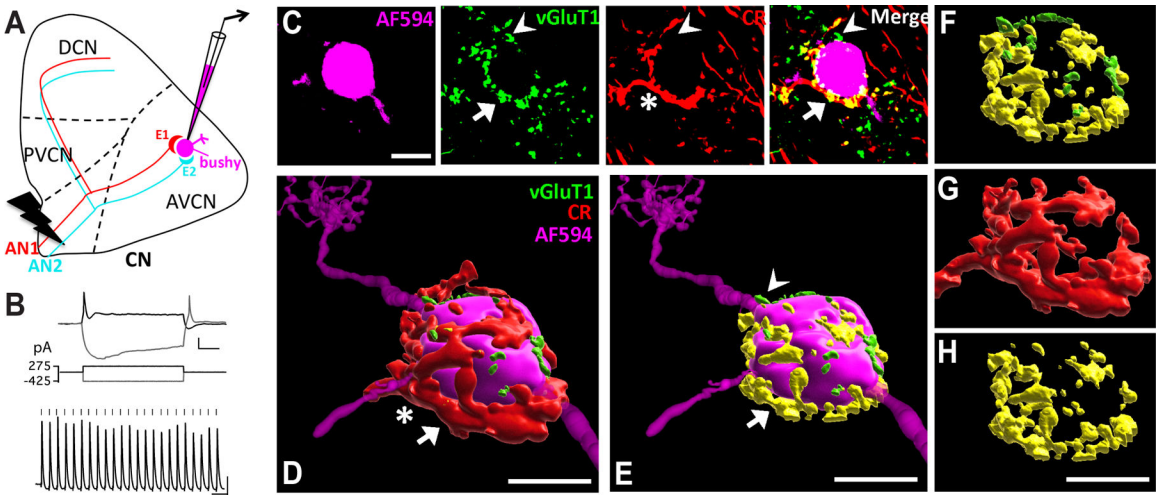

Figure 2. Different subtypes of AN synapses converge onto individual CN neurons.

(**A**) Diagram of the CN and experimental setup. It depicts two endbulb of Held synapses (E1 and E2) from different AN fibers (AN1 and AN2) that innervate the target bushy neuron, which is recorded and filled with fluorescent dye (magenta). AN is activated by electric stimulation. CN: cochlear nucleus; AVCN: anteroventral CN; PVCN: posteroventral CN; DCN: dorsal CN.

(**B**) Example responses of a bushy neuron to current step injections (top) and trains of AN stimulation at 100 Hz (bottom). Ticks mark the stimulus onset. Scale: 10 mV and 20 ms.

(**C**) Single frame confocal images of the bushy neuron in (**B**) filled with Alexa Fluor 594 dye (magenta), with immunostained VGluT1 (green) and calretinin (CR; red). The bushy neuron receives a large type I_a endbulb of Held synapse (asterisk), which contains VGluT1-labeled puncta (arrow). Double-labeled puncta are shown in yellow in the merged panel (arrow). VGluT1-labeled puncta that do not overlap with CR staining are shown in green in the merged panel (arrowhead), which are from AN synapses that do not express calretinin (non-type I_a synapse). Scale: 10 μm.

(**D**) 3D reconstruction of the bushy neuron and AN synapses in (**C**). Red: CR-stained type I_a endbulb of Held synapse. Scale: 10 μm, also applies to **E-H.** See also Supplemental Video 1.

(**E**) same as in (**D**) except showing only the VGluT1-labeled puncta. Yellow (arrow): VGluT1-labeled puncta inside the calretinin-expressing type I_a synapses; green (arrowhead): puncta from non-calretinin-expressing (non-type I_a) synapses.

(**F**) View of all VGluT1-labeled puncta from (**E**) without revealing the postsynaptic bushy neuron. Note that this bushy neuron received mostly type I_a synaptic inputs from the AN in terms of VGluT1-labeled puncta volume.

(**G**) Morphology of the single type I_a endbulb of Held synapse from (**D**).

(**H**) Type I_a VGluT1-labeled puncta inside the single endbulb in (**G**).

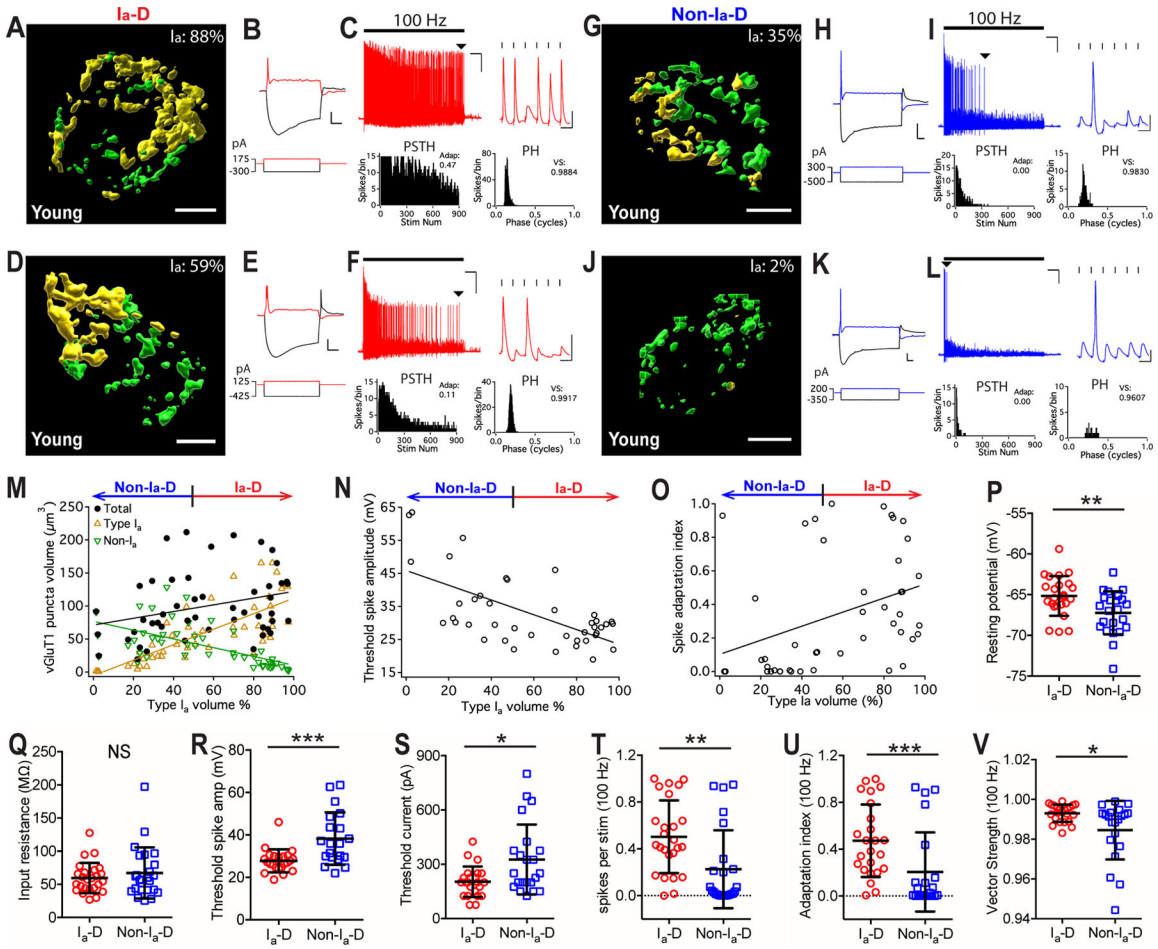

Figure 3. The proportion of type I_a synaptic inputs correlates with physiological properties of postsynaptic neurons in young mice.

(**A-C**) An example bushy neuron that received mostly type I_a synaptic inputs (I_a-dominant, or I_a-D) from the AN. (**A**) Reconstructed VGluT1-labeled puncta surrounding the soma of the target bushy cell (not shown) from type I_a (yellow) and non-type I_a (green) synapses. I_a %: volume proportion of the VGluT1-labeled puncta from type I_a synapses over total. Scale: 5 μm. (**B**) Responses of the bushy cell to current step injections. Red traces: threshold current injection (bottom) and response (top). Scale: 10 mV and 20 ms. (**C**) The neuron fired sustained spikes to a train of auditory nerve stimulation (black bar) at 100 Hz; scale: 10 mV and 1 s. Arrowhead: last spikes of the train expanded in the inset on the right; scale: 10 mV and 10 ms. PSTH: post-stimulus time histogram. Stim Num: stimulus number. Adap: spike adaptation index. PH: period histogram. VS: vector strength.

(**D-F**) Another example bushy neuron with I_a-D but lower proportion of type I_a inputs.

(**G-I**, **J-L**) Two example bushy neurons that received mostly non-type I_a synaptic inputs (Non-type I_a-dominant, or Non-I_a-D), and fired only transient or onset spikes to AN stimulus trains.

(**M**) Bushy neurons with different proportion of type I_a inputs (x-axis) show correlated distribution in the total volume of VGluT1-labeled puncta (black), volume of type I_a only

puncta (yellow), and volume of non-type I_a only puncta (green). Linear regression lines: black, $r^2 = 0.09$, $p = 0.039$; yellow, $r^2 = 0.57$, $p < 0.0001$; green, $r^2 = 0.38$, $p < 0.0001$.
(**N**) The proportion of type I_a inputs (x-axis) in bushy neurons negatively correlates with their threshold spike amplitude, as shown by example responses in **B**, **E**, **H** and **K**. Linear regression line: $r^2 = 0.40$, $p < 0.0001$.
(**O**) Bushy neurons with different proportion of type I_a inputs (x-axis) show different firing patterns to 100 Hz stimulus trains, as quantified by spike adaptation index. Linear regression line: $r^2 = 0.13$, $p = 0.015$.
(**P-V**) Comparisons between bushy neurons with I_a-D and Non-I_a-D inputs in resting potential (**P**), input resistance (**Q**), threshold spike amplitude (**R**), threshold current injection level that triggered the first spike (**S**), firing rate throughout the 100 Hz train (**T**), spike adaptation index (**U**), and vector strength of the spikes (**V**). Unpaired t-test or Mann-Whitney test: NS, $p > 0.05$; *$p < 0.05$; **$p < 0.01$; ***$p < 0.001$.

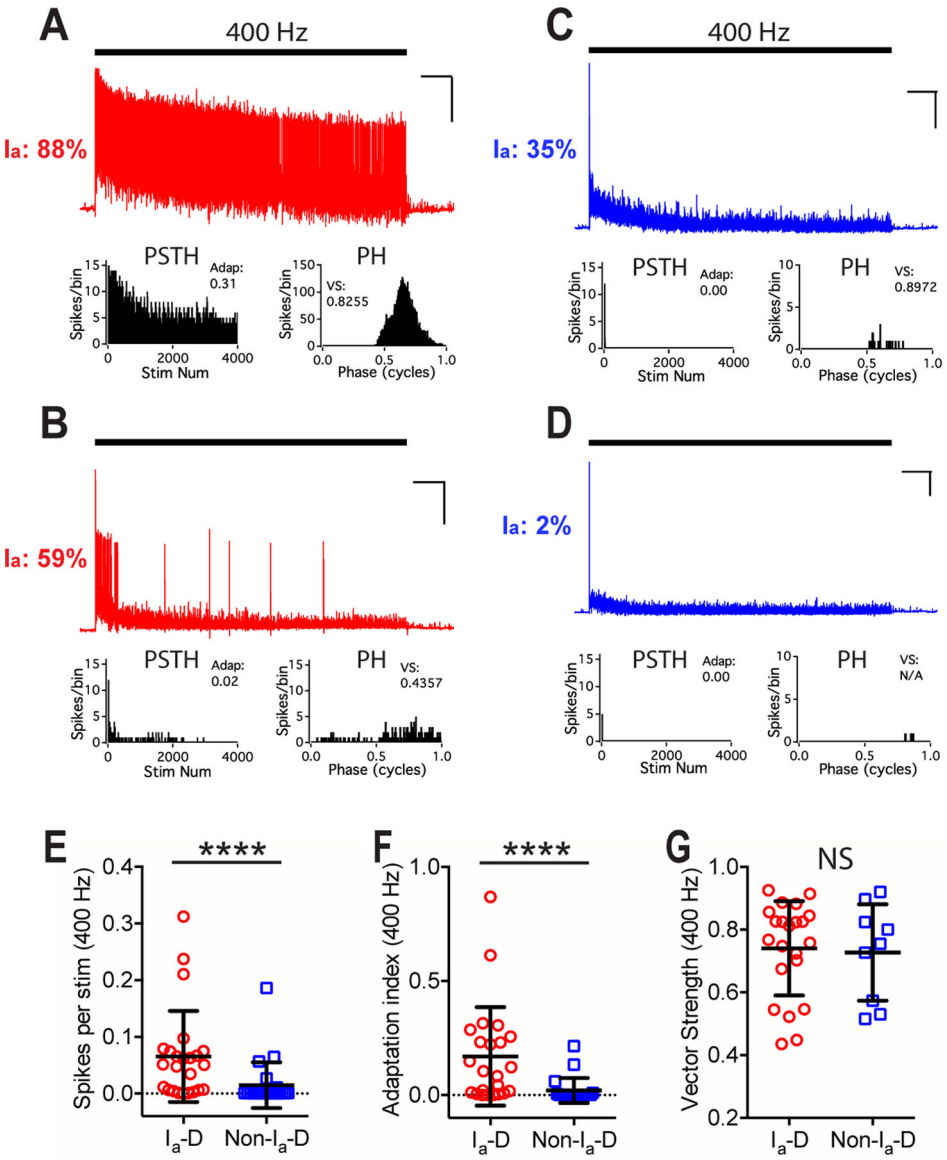

Figure 4. Bushy neurons with different convergence of AN synaptic inputs show different firing patterns to trains of AN stimulation at 400 Hz in young mice.

(**A**) The same example bushy neuron in Fig. 3A fired sustained spikes to trains of AN stimulation at 400 Hz. Scale: 10 mV and 1 s.

(**B-D**) Responses of bushy neurons in Fig. 3D, **G**, and **J** to AN stimulation at 400 Hz. Vector strength of the cell in **D** was not calculated due to insufficient number of spikes.

(**E-G**) Comparisons between bushy neurons with I_a-D inputs and Non-I_a-D inputs to 400 Hz AN stimulus trains in firing rate (**E**), spike adaptation index (**F**), and vector strength (**G**). Unpaired t-test or Mann Whitney test: NS, $p > 0.05$; ****$p < 0.0001$.

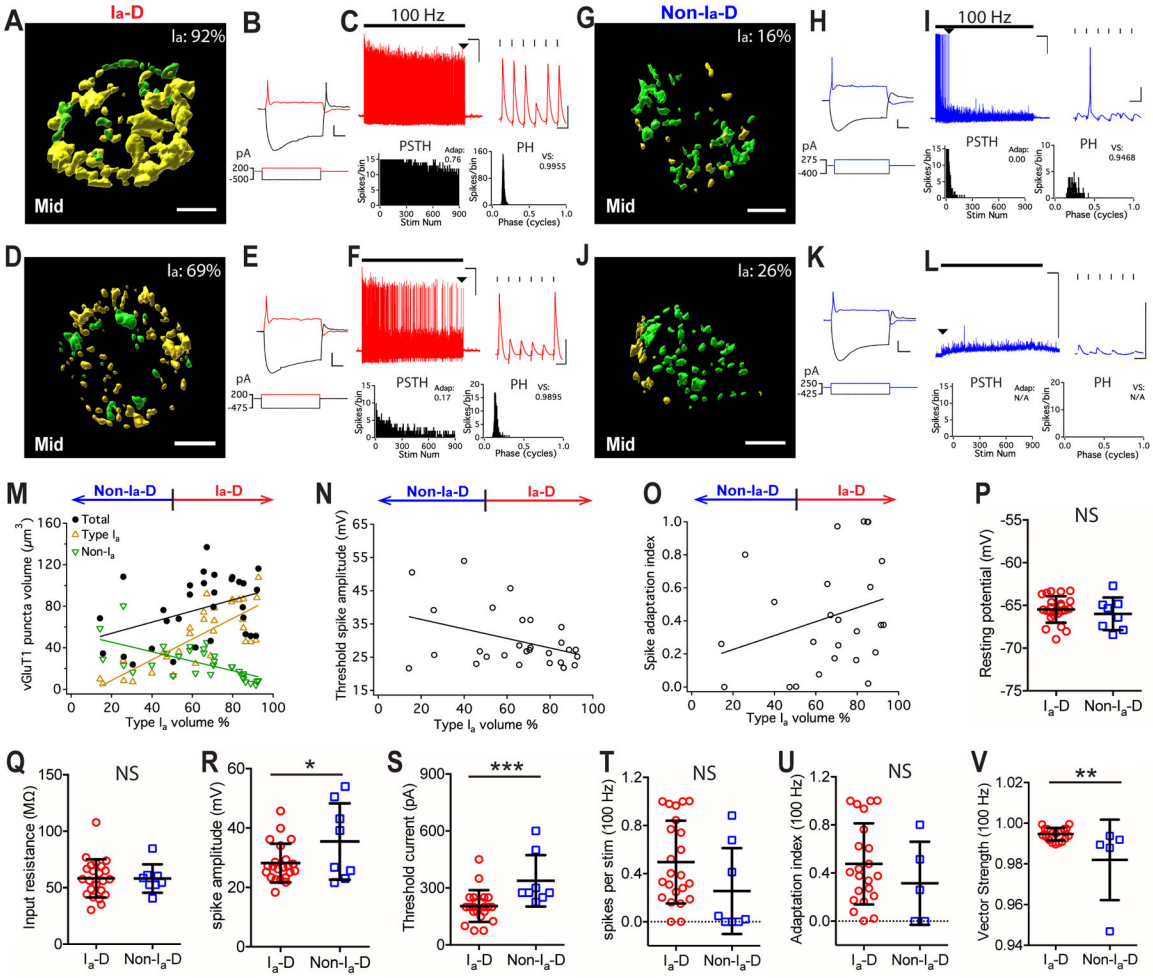

Figure 5. Convergence of different AN synapses and the response properties of postsynaptic bushy neurons in middle-aged mice

(**A-C**) Example bushy neuron with I_a-D inputs (I_a: 92%). (**A**) Reconstructed VGluT1-labeled puncta from type I_a (yellow) and non-type I_a (green) synapses. Scale: 5 μm. (**B**) Responses of the bushy cell to current step injections. Scale: 10 mV and 20 ms. (**C**) The neuron fired sustained spikes to a train of auditory nerve stimulation at 100 Hz; scale: 10 mV and 1 s. Arrowhead: last spikes of the train expanded in the inset on the right; scale: 10 mV and 10 ms.

(**D-F**) Example bushy neuron with I_a-D but lower proportion of type I_a inputs (I_a: 69%).

(**G-I**, **J-L**) Two example bushy neurons that received Non-I_a-D inputs, and fired only transient spikes or failed to fire any spike to AN stimulus trains.

(**M**) Bushy neurons with different proportion of type I_a inputs show correlated distribution in the total volume of VGluT1-labeled puncta (black), volume of type I_a only puncta (yellow), and volume of non-type I_a only puncta (green). Linear regression lines: black, $r^2 = 0.16$, $p = 0.025$; yellow, $r^2 = 0.62$, $p < 0.0001$; green, $r^2 = 0.40$, $p = 0.0001$.

(**N**) The proportion of type I_a inputs in bushy neurons negatively correlates with their threshold spike amplitude. Linear regression line: $r^2 = 0.15$, $p = 0.043$.

(**O**) Spike adaptation index from 100 Hz trains in bushy neurons with different proportion of type I_a inputs. Linear regression line: $r^2 = 0.08$, $p = 0.160$.

(**P-V**) Comparisons between bushy neurons from middle-aged mice with I_a-D and Non-I_a-D inputs in resting potential (**P**), input resistance (**Q**), threshold spike amplitude (**R**), threshold current level (**S**), firing rate throughout the 100 Hz train (**T**), spike adaptation index (**U**), and vector strength of the spikes (**V**). Unpaired t-test or Mann-Whitney test: NS, $p > 0.05$; *$p < 0.05$; **$p < 0.01$; ***$p < 0.001$.

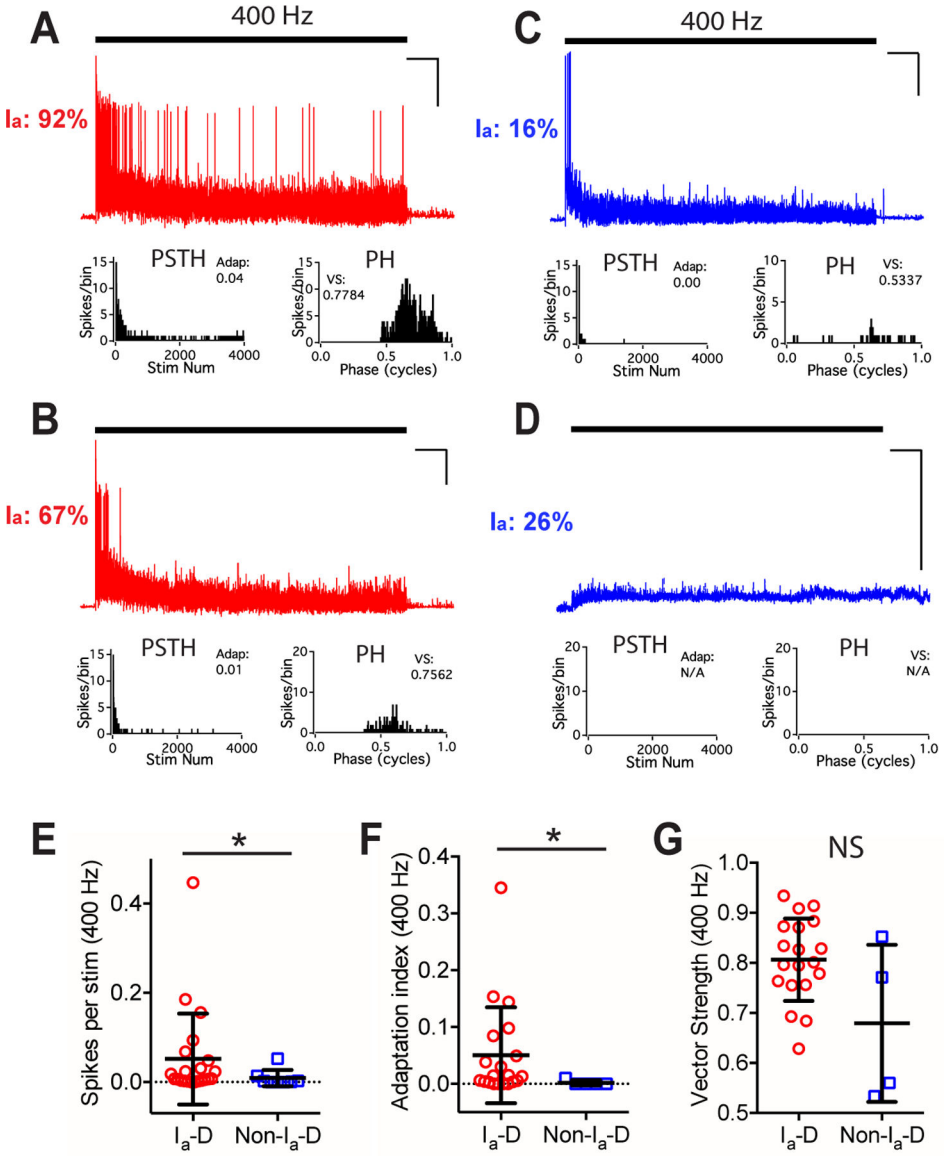

Figure 6. Bushy neurons in middle-aged mice show different firing properties to trains of AN stimulation at 400 Hz.

(**A-D**) Responses of four example bushy neurons to trains of AN stimulation at 400 Hz. Scale: 10 mV and 1 s. No spike was evoked in the cell in **D**.

(**E-G**) Comparisons between bushy neurons with I_a-D and Non-I_a-D inputs to 400 Hz AN stimulus trains in firing rate (**E**), spike adaptation index (**F**), and vector strength (**G**). Mann Whitney test: NS, $p > 0.05$; *$p < 0.05$.

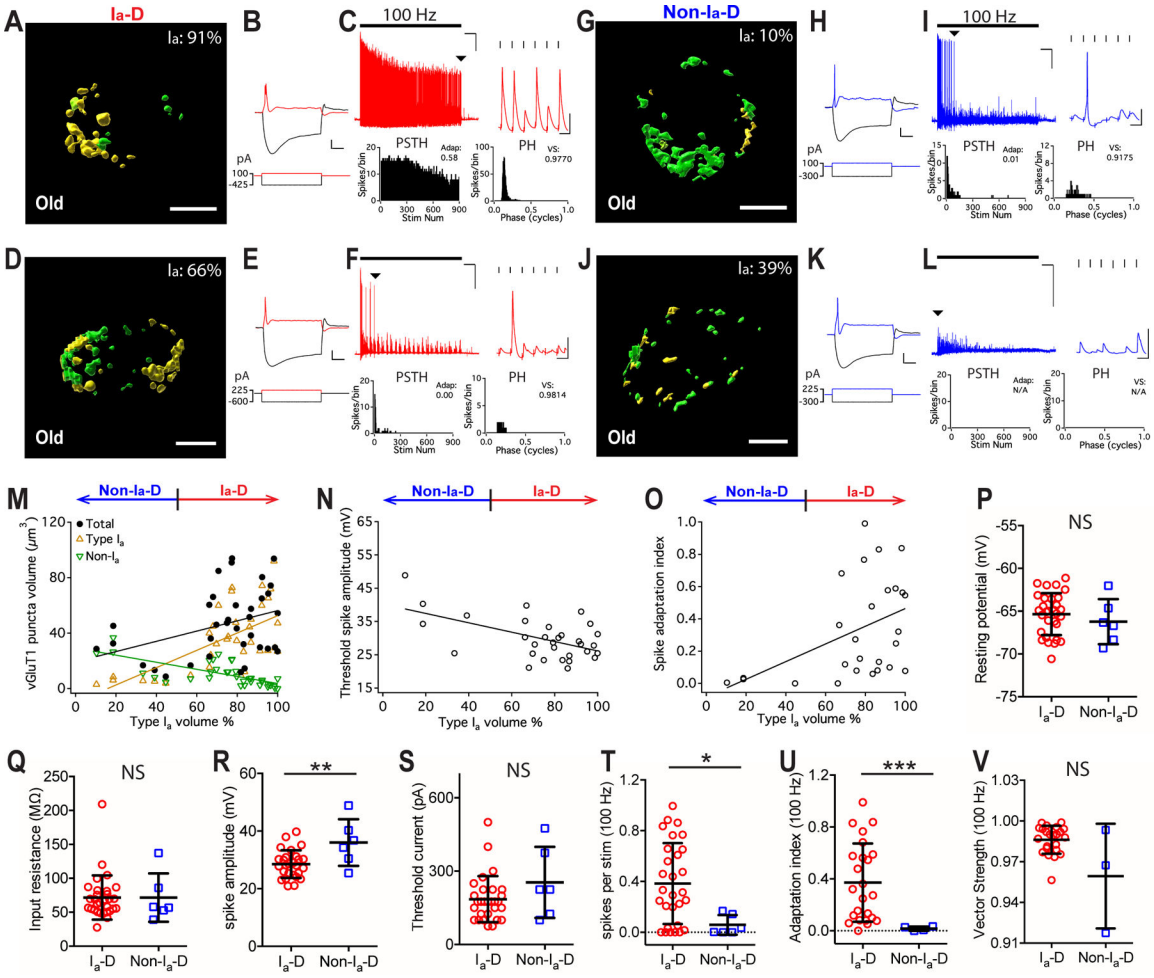

Figure 7. Convergence of different AN synapses and the response properties of postsynaptic bushy neurons in old mice

(**A-C**) Example bushy neuron with I_a-D inputs (I_a: 91%). (**A**) Reconstructed VGluT1-labeled puncta from type I_a (yellow) and non-type I_a (green) synapses. Scale: 5 μm. (**B**) Responses of the bushy cell to current step injections. Scale: 10 mV and 20 ms. (**C**) The neuron fired sustained spikes to a train of auditory nerve stimulation at 100 Hz; scale: 10 mV and 1 s. Arrowhead: last spikes of the train expanded in the inset on the right; scale: 10 mV and 10 ms.

(**D-F**) Example bushy neuron with I_a-D but lower proportion of type I_a inputs (I_a: 66%).

(**G-I**, **J-L**) Two example bushy neurons that received Non-I_a-D inputs (I_a: 10% and 39%).

(**M**) Bushy neurons with different proportion of type I_a inputs show correlated distribution in the total volume of VGluT1-labeled puncta (black), volume of type I_a only puncta (yellow), and volume of non-type I_a only puncta (green). Linear regression lines: black, $r^2 = 0.13$, $p = 0.033$; yellow, $r^2 = 0.40$, $p < 0.0001$; green, $r^2 = 0.49$, $p < 0.0001$.

(**N**) Proportion of type I_a inputs (x-axis) in bushy neurons negatively correlates with their threshold spike amplitude. Linear regression line: $r^2 = 0.30$, $p = 0.001$.

(**O**) Spike adaptation index from 100 Hz trains in bushy neurons with different proportion of type I_a inputs (x-axis). Linear regression line: $r^2 = 0.20$, $p = 0.019$.

(**P-V**) Comparisons between bushy neurons from old mice with I_a-D and Non-I_a-D inputs in resting potential (**P**), input resistance (**Q**), threshold spike amplitude (**R**), threshold current level (**S**), firing rate throughout the 100 Hz trains (**T**), spike adaptation index (**U**), and vector strength of the spikes (**V**). Unpaired t-test or Mann-Whitney test: NS, $p > 0.05$; *$p < 0.05$; ***$p < 0.001$.

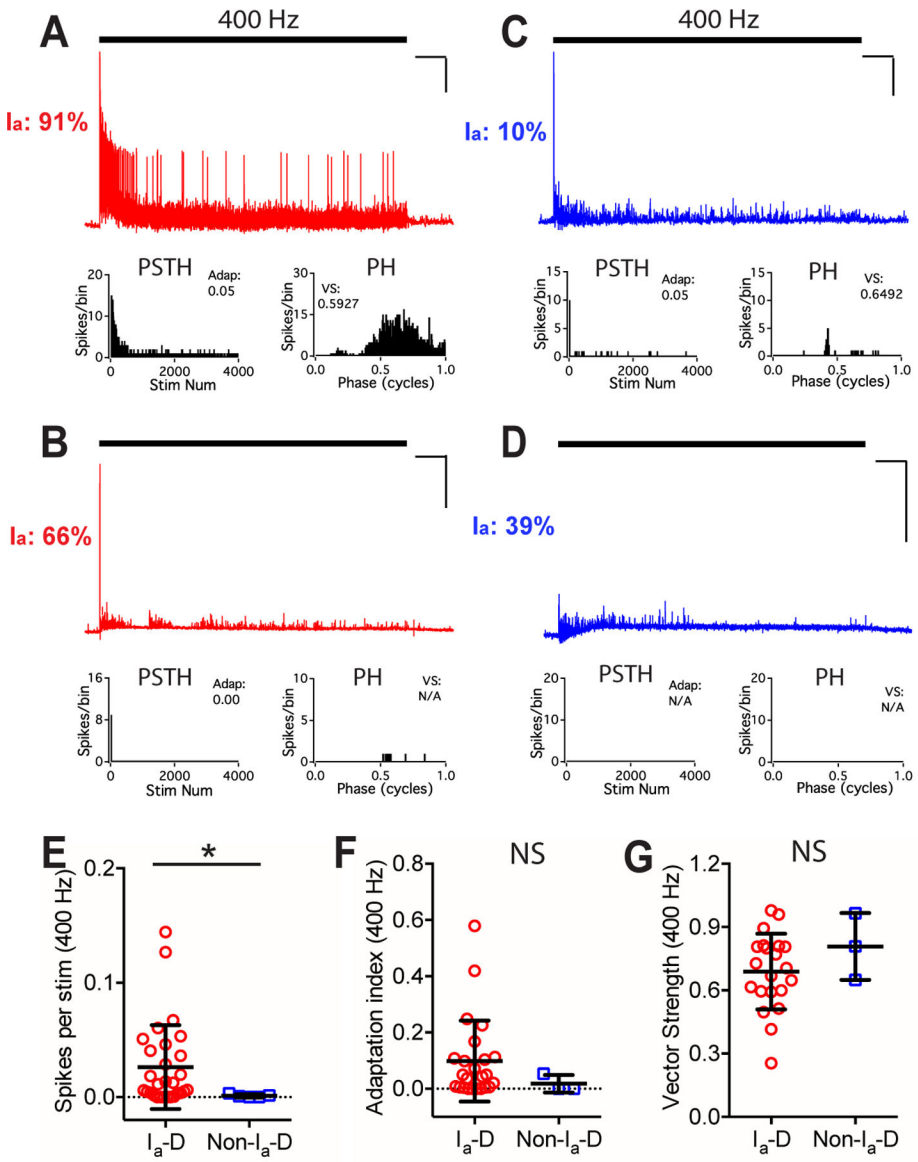

Figure 8. Bushy neurons in old mice show different firing properties to trains of AN stimulation at 400 Hz.

(**A-D**) Responses of four example bushy neurons to trains of AN stimulation at 400 Hz. Scale: 10 mV and 1 s. No spike was evoked in the cell in **D**.

(**E-G**) Comparisons between bushy neurons with I_a-D and Non-I_a-D inputs to 400 Hz AN stimulus trains in firing rate (**E**), spike adaptation index (**F**), and vector strength (**G**). Mann Whitney test: NS, $p > 0.05$; *$p < 0.05$.

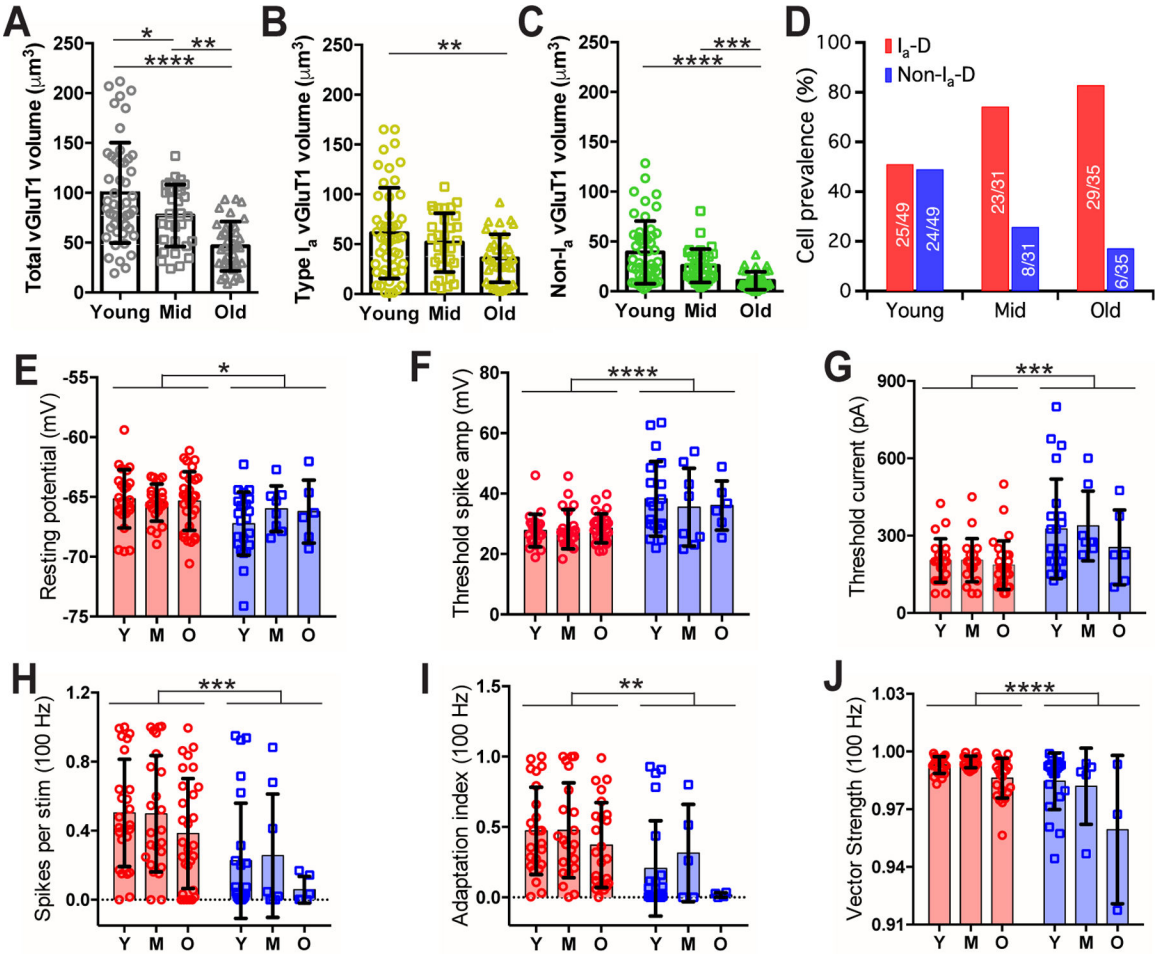

Figure 9. AN central synaptopathy is more severe in non-type I_a synapses and associated with altered composition of bushy neuron population during ARHL

(**A-C**) Comparisons of the total volume (**A**), type I_a only volume (**B**) and non-type I_a only volume (**C**) of VGluT1-labeled puncta onto bushy neurons from three age groups of mice. Tukey's or Dunn's multiple comparison tests: *$p < 0.05$; **$p < 0.01$; ***$p < 0.001$; ****$p < 0.0001$.

(**D**) Prevalence of bushy neurons that receive I_a-D and Non-I_a-D synaptic inputs among three age groups. Numbers mark the cell count of each type over total.

(**E-J**) Comparisons of bushy neurons among three age groups in resting potential (**E**), threshold spike amplitude (**F**), threshold current injection that triggered the first spike (**G**), firing rate to 100 Hz stimulation (**H**), spike adaptation index (**I**), and vector strength of the spikes throughout the 100 Hz trains (**J**). Two-way ANOVA revealed significant cell type effect (I_a-D vs. Non-I_a-D) in all panels (**E-J**): **$p < 0.01$; ***$p < 0.001$; ****$p < 0.0001$. Age effect was only significant in vector strength (**J**): $p < 0.001$.

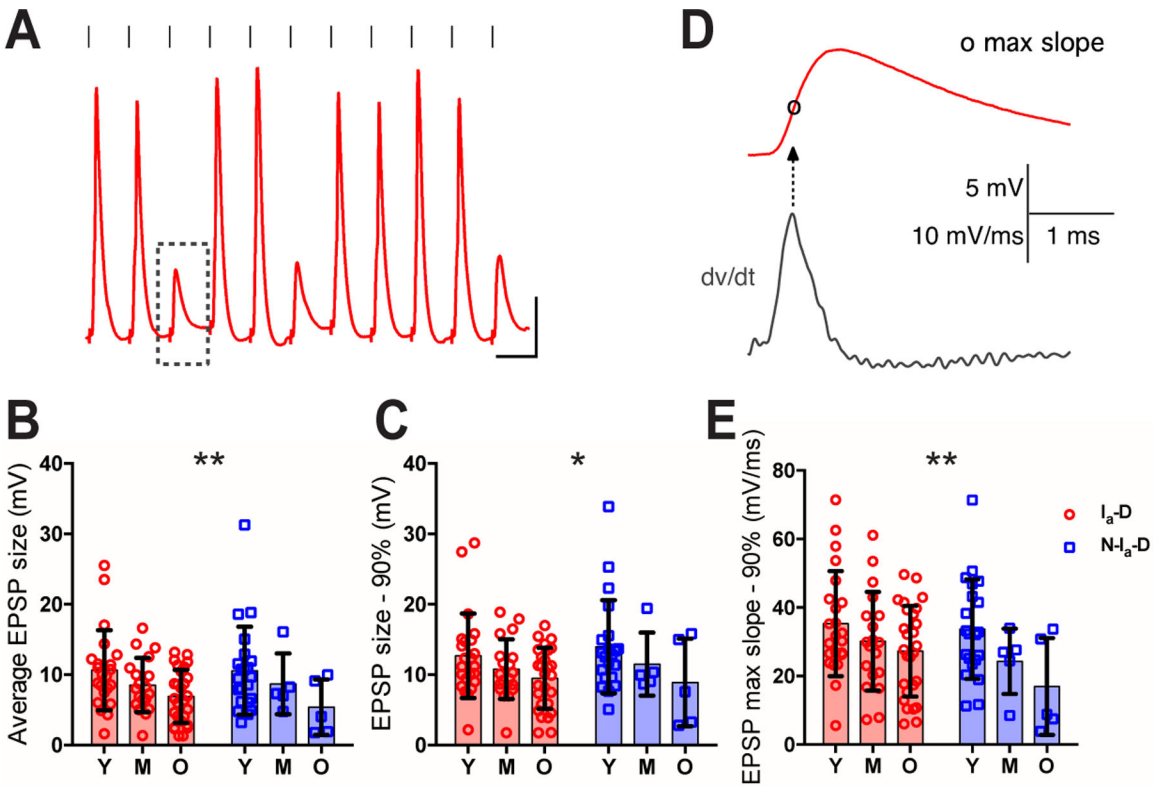

Figure 10. Evoked EPSPs decrease in amplitude with age during ARHL.

(**A**) Example response of a bushy neuron to show AN stimulation evoked spikes and EPSPs. Dashed rectangle: an example EPSP that failed to trigger any spike. Scale: 10 mV and 10 ms.

(**B-C**) Comparisons of bushy neurons among three age groups in average amplitude of EPSPs that failed to trigger spikes (**B**), and EPSP amplitude at 90th percentile (**C**).

(**D**) Maximum rising slope of the example EPSP from (**A**), calculated as the peak of the first derivative (dv/dt) during the rising phase.

(**E**) Comparison of EPSP maximum slope at 90th percentile.

Two-way ANOVA revealed significant age effect (I_a-D vs. Non-I_a-D) in **B, C** and **E**: *p < 0.05; **p < 0.01.

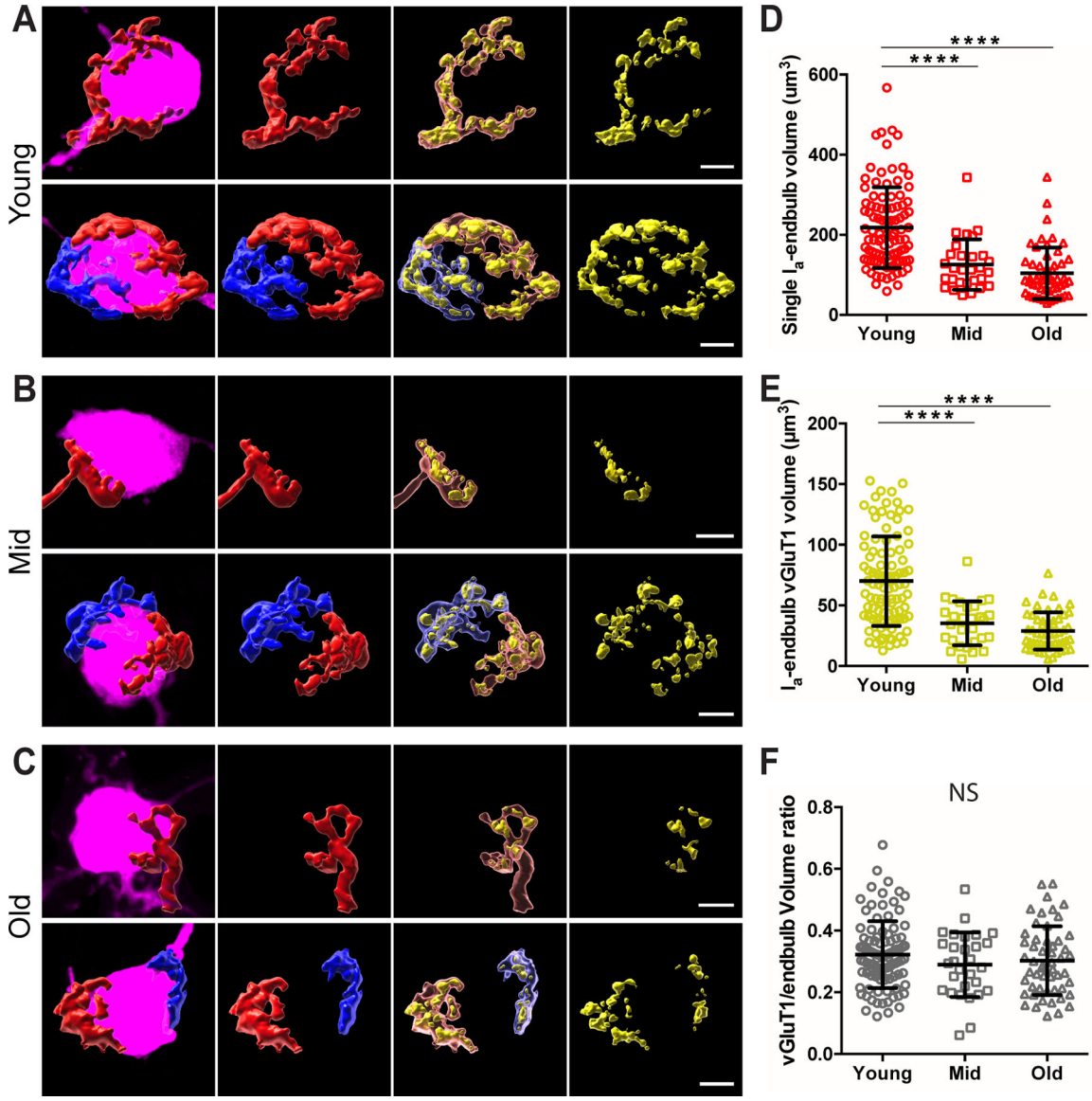

Figure 11. Synaptopathy of individual type I_a endbulb of Held synapses during ARHL.

(**A**) Representative morphology of individual type I_a endbulb of Held synapses in young mice. Panels from left to right: filled neurons (magenta) with reconstructed individual type I_a endbulbs, type I_a endbulbs alone, type I_a endbulbs (semi-transparent) with enclosed VGluT1-labled puncta (yellow), and VGluT1-labeled puncta alone. Top panels: example bushy neuron with only one type I_a endbulb of Held synapse. Bottom panels: example neuron with two type I_a endbulb of Held synapses, which are shown in red and blue respectively.

(**B**) Representative morphology of individual type I_a endbulb of Held synapses in middle-aged mice.

(**C**) Representative morphology of individual type I_a endbulb of Held synapses in old mice. Scales in **A-C**: 5 µm.

(**D**-**F**) Comparisons of individual type I_a endbulb volume (**D**), enclosed VGluT1-puncta volume (**E**), and VGluT1/endbulb volume ratio (**F**) among three age groups. Dunn's multiple comparison test: NS, $p > 0.05$; ****$p < 0.0001$.

Table 1.

Electrophysiological properties of bushy neurons.

		Ia-D			Non-Ia-D			p value (unpaired t-test or *Mann Whitney test*)
		n	mean	SD	n	mean	SD	
Young	resting potential (mV)	25	−65.2	2.4	24	−67.2	2.6	0.0075**
	input resistance (MΩ)	25	60	23	24	67	38	*0.851*
	threshold spike amp (mV)	25	27.8	5.4	24	38.3	12.4	0.0007***
	threshold current (pA)	25	203	84	24	326	193	*0.025**
	spikes per stim at 100 Hz	25	0.50	0.31	24	0.23	0.33	*0.0014***
	adaptation index at 100 Hz	25	0.47	0.31	24	0.21	0.34	*0.0004****
	vector strength at 100 Hz	25	0.993	0.004	24	0.985	0.015	*0.030**
	spike jitter at 100 Hz (ms)	25	0.180	0.060	24	0.257	0.126	*0.030**
	spikes per stim at 400 Hz	23	0.068	0.080	21	0.016	0.042	*< 0.0001****
	adaptation index at 400 Hz	23	0.17	0.22	21	0.02	0.05	*< 0.0001****
	vector strength at 400 Hz	22	0.74	0.15	9	0.73	0.15	0.823
	spike jitter at 400 Hz (ms)	22	0.344	0.181	9	0.347	0.164	*0.781*
Middle-aged	resting potential (mV)	23	−65.5	1.6	8	−66.0	1.9	0.449
	input resistance (MΩ)	23	58	17	8	58	13	0.982
	threshold spike amp (mV)	23	28.2	6.5	8	35.5	12.9	0.049*
	threshold current (pA)	23	205	84	8	338	136	*0.0005****
	spikes per stim at 100 Hz	23	0.50	0.34	8	0.26	0.36	0.080
	adaptation index at 100 Hz	22	0.48	0.34	5	0.32	0.35	0.306
	vector strength at 100 Hz	20	0.995	0.003	5	0.982	0.020	*0.0074***
	spike jitter at 100 Hz (ms)	20	0.166	0.069	5	0.279	0.142	*0.015**
	spikes per stim at 400 Hz	22	0.05	0.10	8	0.01	0.02	*0.030**
	adaptation index at 400 Hz	20	0.035	0.049	5	0.002	0.005	*0.025**
	vector strength at 400 Hz	19	0.806	0.082	4	0.679	0.157	*0.138*
	spike jitter at 400 Hz (ms)	19	0.267	0.079	4	0.381	0.155	*0.188*
Old	resting potential (mV)	29	−65.3	2.5	6	−66.2	2.6	0.445
	input resistance (MΩ)	29	72	33	6	72	36	*0.982*
	threshold spike amp (mV)	29	28.5	4.8	6	36.0	8.1	0.0047**
	threshold current (pA)	29	185	94	6	254	145	*0.273*
	spikes per stim at 100 Hz	29	0.38	0.32	6	0.06	0.08	0.019*
	adaptation index at 100 Hz	24	0.37	0.30	4	0.02	0.02	*0.0007****
	vector strength at 100 Hz	23	0.986	0.010	3	0.959	0.039	*0.182*
	spike jitter at 100 Hz (ms)	23	0.257	0.118	3	0.420	0.241	*0.211*
	spikes per stim at 400 Hz	29	0.026	0.037	5	0.001	0.001	*0.018**
	adaptation index at 400 Hz	24	0.098	0.144	3	0.018	0.031	*0.230*
	vector strength at 400 Hz	21	0.689	0.179	3	0.808	0.158	*0.271*
	spike jitter at 400 Hz (ms)	21	0.361	0.154	3	0.247	0.131	*0.172*